

Inverse wave-number-dependent source problems for the Helmholtz equation

Hongxia Guo* Guanghui Hu†

Abstract

This paper is concerned with the multi-frequency factorization method for imaging the support of a wave-number-dependent source function. It is supposed that the source function is given by the Fourier transform of some time-dependent source with a priori given radiating period. Using the multi-frequency far-field data at a fixed observation direction, we provide a computational criterion for characterizing the smallest strip containing the support and perpendicular to the observation direction. The far-field data from sparse observation directions can be used to recover a Θ -convex polygon of the support. The inversion algorithm is proven valid even with multi-frequency near-field data in three dimensions. The connections to time-dependent inverse source problems are discussed in the near-field case. We also comment on possible extensions to source functions with two disconnected supports. Numerical tests in both two and three dimensions are implemented to show effectiveness and feasibility of the approach. This paper provides numerical analysis for a frequency-domain approach to recover the support of an admissible class of time-dependent sources.

Keywords: Inverse source problem, Helmholtz equation, wave-number-dependent sources, multi-frequency data, factorization method.

1 Introduction and problem formulation

Consider the time-dependent acoustic wave radiating from a source term in an isotropic and homogeneous medium

$$\begin{aligned} \partial_t^2 U(x, t) &= \Delta U(x, t) + S(x, t), & (x, t) &\in \mathbb{R}^3 \times \mathbb{R}_+, \\ U(x, 0) &= \partial_t U(x, 0) = 0, & x &\in \mathbb{R}^3, \end{aligned} \tag{1.1}$$

where $\text{supp } S(x, t) = D \times (t_{\min}, t_{\max}) \subset \mathbb{R}^3 \times \mathbb{R}_+$ with $t_{\max} > t_{\min} \geq 0$. The wave speed in the background medium has been normalized to be one. We suppose that $D \subset \mathbb{R}^3$ is a bounded

*School of Mathematical Sciences and LEMP, Nankai University, 300071 Tianjin, China. (hxguo@nankai.edu.cn)

†Corresponding author: School of Mathematical Sciences and LEMP, Nankai University, 300071 Tianjin, China. (ghhu@nankai.edu.cn)

Lipschitz domain such that $\mathbb{R}^3 \setminus \overline{D}$ is connected and that $S(x, t) \in C([t_{\min}, t_{\max}], L^\infty(D))$ is a real-valued function fulfilling the coercivity constraint

$$S(x, t) \geq c_0 > 0 \quad \text{a.e. } x \in \overline{D}, \quad t \in (t_{\min}, t_{\max}). \quad (1.2)$$

The above condition (1.2) implies that the shape and location of the time-dependent source S does not vary along with the time variable. The time interval $(t_{\min}, t_{\max}) \subset \mathbb{R}_+$ represents the duration period for source radiating. The solution U can be given explicitly as the convolution of the fundamental solution to the wave equation with the source term, that is,

$$U(x, t) = G(x, t) * S(x, t) := \int_{\mathbb{R}_+} \int_{\mathbb{R}^3} G(x - y; t - \tau) S(y, \tau) dy d\tau \quad (1.3)$$

where

$$G(x, t) = \frac{\delta(t - |x|)}{4\pi|x|}, \quad x \in \mathbb{R}^3 \setminus \{0\}, \quad t \in \mathbb{R}_+, \quad t \neq |x|.$$

Taking the Fourier transform of $U(x, t)$ with respect to the time variable, one deduces from (1.3) that

$$w(x, k) := \frac{1}{\sqrt{2\pi}} \int_{\mathbb{R}} U(x, t) e^{-ikt} dt = \frac{1}{\sqrt{2\pi}} \int_{\mathbb{R}_+} U(x, t) e^{-ikt} dt = \int_{\mathbb{R}^3} \Phi_k(x, y) f(y, k) dy, \quad (1.4)$$

where $\Phi_k(x, y)$ and $f(y, k)$ denote respectively the Fourier transforms of the fundamental solution $G(x - y; t)$ and $S(y, t)$. By the wave equation of the fundamental solution $G(x, t)$,

$$\begin{aligned} \partial_t^2 G(x - y, t) - \Delta G(x - y, t) &= \delta(x - y) \delta(t), & x \in \mathbb{R}^3 \setminus \{y\}, \quad t > 0, \\ G(x - y, 0) = \partial_t G(x - y, 0) &= 0, & x \in \mathbb{R}^3 \setminus \{y\}, \end{aligned}$$

we conclude that $\Phi_k(x, y)$ coincides with the fundamental solution to the Helmholtz equation $(\Delta + k^2)w = 0$, given by

$$\Phi_k(x, y) = \frac{e^{ik|x-y|}}{4\pi|x-y|}, \quad x \neq y, \quad x, y \in \mathbb{R}^3.$$

It is well known that $\Phi_k(x, y)$ satisfies the Sommerfeld radiation condition. By the assumption of S , we have

$$f(x, k) = \frac{1}{\sqrt{2\pi}} \int_{\mathbb{R}} S(x, t) e^{-ikt} dt = \frac{1}{\sqrt{2\pi}} \int_{t_{\min}}^{t_{\max}} S(x, t) e^{-ikt} dt, \quad (1.5)$$

which is compactly supported on \overline{D} with respect to the space variables. Moreover, $f(\cdot, k) \in L^2(D)$ for any $k > 0$. Therefore, it follows from (1.4) that $w(\cdot, k) \in H_{loc}^2(\mathbb{R}^3)$ satisfies

$$\Delta w(x, k) + k^2 w(x, k) = -f(x, k), \quad x \in \mathbb{R}^3, \quad k > 0, \quad (1.6)$$

$$\lim_{r \rightarrow \infty} r(\partial_r w - ikw) = 0, \quad r = |x|, \quad (1.7)$$

where the limit (1.7) holds uniformly in all directions $\hat{x} = x/|x| \in \mathbb{S}^2 := \{x \in \mathbb{R}^3 : |x| = 1\}$. The Sommerfeld radiation condition (1.7) gives rise to the following asymptotic behavior at infinity:

$$w(x) = \frac{e^{ik|x|}}{4\pi|x|} \left\{ w^\infty(\hat{x}, k) + O\left(\frac{1}{r}\right) \right\} \quad \text{as } |x| \rightarrow \infty, \quad (1.8)$$

where $w^\infty(\cdot, k) \in C^\infty(\mathbb{S}^2)$ is referred to as the far-field pattern (or scattering amplitude) of w . It is well known that the function $\hat{x} \mapsto w^\infty(\hat{x}, k)$ is real analytic on \mathbb{S}^2 , where $\hat{x} \in \mathbb{S}^2$ is usually called the observation direction. By (1.4), the far-field pattern w^∞ of w can be expressed as

$$w^\infty(\hat{x}, k) = \int_D e^{-ik\hat{x}\cdot y} f(y, k) dy, \quad \hat{x} \in \mathbb{S}^2, \quad k > 0. \quad (1.9)$$

Noting that the time-dependent source S is real valued, we have $f(x, -k) = \overline{f(x, k)}$ and thus $w^\infty(\hat{x}, -k) = \overline{w^\infty(\hat{x}, k)}$ for all $k > 0$.

Let $0 \leq k_{\min} < k_{\max}$ and denote by (k_{\min}, k_{\max}) the bandwidth of wave-numbers of the Helmholtz equation. In this paper we are interested in the following inverse problem: determine the position and shape of the support D from knowledge of the multi-frequency far-field patterns

$$\{w^\infty(\hat{x}_j, k) : k \in (k_{\min}, k_{\max}), j = 1, 2, \dots, J\}.$$

We shall establish a factorization method for imaging D from sparse far-field measurements at multiple frequencies.

If the source term is independent of frequencies (which corresponds to the critical case that $S(x, t) = s(x)\delta(t)$ and $f(x, k) = s(x)$; see Remark 4.1), the far-field pattern given by (1.9) is nothing else but the Fourier transform of the space-dependent source term f at the Fourier variable $\xi = k\hat{x} \in \mathbb{R}^3$ multiplied by some constant. Since f is compactly supported in D , its Fourier transform is analytic in $\xi \in \mathbb{R}^3$. Hence, the far-field measurements over an interval of frequencies and observation directions uniquely determine the source function and also its support. A wide range of literature is devoted to inverse wavenumber-independent source problems with multi-frequency data, for example, uniqueness proofs and increasing stability analysis with near-field measurements [3, 4, 8, 11, 31] and a couple of numerical schemes such as iterative method, Fourier method and test-function method for recovering the source function [3, 5, 11, 37] and sampling-type methods for imaging the support [2, 13, 27]. On the other hand, the inverse source problem with the measurement data at a single frequency becomes severely ill-posed. It is impossible in general to determine a source function (even its support) from a single far-field pattern due to the existence of non-radiating sources; see e.g., [6, 9, 10] for non-uniqueness examples. In a series papers by Kusiak and Sylvester [30, 35, 36], the concept of convex scattering support has been introduced to define the smallest convex set that carries a single far-field pattern. It was shown in [7, 20] that a convex-polygonal source support and an admissible class of analytic source functions can be uniquely determined by a single far-field pattern. Numerical schemes such as the enclosure method [24] and one-wave factorization method [32] were proposed for imaging the

support of such convex-polygonal sources. The filtered backprojection method [16, 17] and a hybrid method involving iterative and range test [1] were also investigated with a single far-field measurement.

In contrast to vast literatures for space-dependent source terms, little is known if the source function depends on both frequency/wave-number and spatial variables. Here we assume that the dependence on the frequency is unknown. In one of the author's previous work [2], a direct imaging method was examined for recovering the support of a wave-number-dependent source, but numerical solutions are not satisfactory in comparison with the results for wavenumber-independent sources. One can see the essential difficulties from the expression (1.9), where the far-field pattern is no longer the Fourier transform of the source function. Hence, most existing methods cannot be straightforwardly carried over to frequency-number-dependent source terms. In this paper, we consider an inverse frequency-dependent source problem originating from inverse time-dependent source problems. The temporal function is supposed to be unknown, but the starting and terminal time points for radiating are given. Consequently, the source term takes a special integral form of the time-dependent source function (see (1.5)) with the a priori given source radiating period (t_{\min}, t_{\max}) . This is motivated by the Fourier method of [21, 22, 23] for proving uniqueness in determining the source function of inhomogeneous hyperbolic equations with vanishing initial data. In these works the inverse time-dependent problems were reduced to equivalent problems in the time-harmonic regime with multi-frequency data. The proposed factorization scheme seems not applicable to general wave-number-dependent sources, because we do not know how to get a desirable factorization form of the far-field operator. Confined by such source functions, we think it is non-trivial to extend our method to inverse medium scattering problems with multi-frequency data. We refer to [12, 14, 15, 19, 25, 26, 34] for the application of the sampling-type methods to nonlinear inverse problems modeled by the Helmholtz equation.

The multi-static factorization method [28, 29], which was proposed by A. Kirsch in 1998, has been extensively studied in various inverse time-harmonic scattering problems using far-field patterns over all observation directions at a fixed frequency. It provides a necessary and sufficient criterion for precisely characterizing the shape and location of a scattering obstacle, utilizing the multi-static spectral system of the far-field operator. The multi-frequency factorization method was rigorously justified in [13] for recovering the smallest strip $K_D^{(\hat{x})}$ that contains the support D of a wave-number-independent source and is orthogonal to the observation direction \hat{x} . Moreover, the Θ -convex polygon of the support can be recovered from the multi-frequency far-field data over sparse observation directions. The aim of this paper is to establish the analogue of the multi-frequency factorization method [13] for imaging the support of a wave-number-dependent source function of the form (1.5). We prove a new range identity for connecting ranges of the far-field operator F and the 'data-to-pattern' operator L . This yields a computational criterion for characterizing the Θ -convex hull of D using the multi-frequency far-field data over sparse observation directions; see Theorem 4.2.

If the near-field measurement data are available in three dimensions, the reconstruction scheme can be used for recovering the minimum and maximum distance between the support and a measurement position. The connection between the near-field factorization method and the time-dependent wave radiating problems will be discussed in Section 4. In two dimensions, the factorization method with far-field data still remains valid, but the near-field version does not hold true any more, perhaps due to the lack of Huygens principle. It is worthy noting that the wave-number-dependence of sources makes this paper quite different from [13]. It is necessary to know the radiating period (t_{\min}, t_{\max}) of the time-dependent source in advance. Physically, this can be explained by the reason that arrival and terminal time points of wave signals at an observation point are available; we refer to Section 4 for the physical interpretation. However, the a priori information on the radiating period (t_{\min}, t_{\max}) can be relaxed to the condition that either t_{\min} or t_{\max} is known and this will be studied in our future works. The reconstruction method considered here can be regarded a frequency-domain method for recovering the support of a time-dependent source fulfilling the coercivity condition (1.2).

The remaining part is organized as follows. In Section 2, the concept of multi-frequency far-field operator is introduced and a new range identity is verified. Section 3 is devoted to the choice of test functions for characterizing the strip $K_D^{(\hat{x})}$ through the 'data-to-pattern' operator L . In Section 4 we define indicator functions using the far-field and near-field data measured at one or several observation directions. We comment on possible extensions of our reconstruction method to source functions with two disconnected supports in Section 5 and numerical tests will be implemented in the final Section 6.

Below we introduce some notations to be used throughout this paper. Unless otherwise stated, we always suppose that D is connected and bounded. Given $\hat{x} \in \mathbb{S}^2$, we define

$$\hat{x} \cdot D := \{t \in \mathbb{R} : t = \hat{x} \cdot y \text{ for some } y \in D\} \subset \mathbb{R}.$$

Hence, $(\inf(\hat{x} \cdot D), \sup(\hat{x} \cdot D))$ must be a finite and connected interval on the real axis. A ball centered at $y \in \mathbb{R}^3$ with the radius $\epsilon > 0$ will be denoted as $B_\epsilon(y)$. For brevity we write $B_\epsilon = B_\epsilon(0)$ when the ball is centered at the origin. Obviously, $\hat{x} \cdot B_\epsilon(y) = (\hat{x} \cdot y - \epsilon, \hat{x} \cdot y + \epsilon)$. In this paper the one-dimensional Fourier and inverse Fourier transforms are defined by

$$(\mathcal{F}f)(k) = \frac{1}{\sqrt{2\pi}} \int_{\mathbb{R}} f(t)e^{-ikt} dt, \quad (\mathcal{F}^{-1}v)(t) = \frac{1}{\sqrt{2\pi}} \int_{\mathbb{R}} v(k)e^{ikt} dt,$$

respectively.

2 Factorization of far-field operator and a new range identity

Following the ideas of [13], we introduce the central frequency k_c and half of the bandwidth of the given data as

$$k_c := \frac{k_{\min} + k_{\max}}{2}, \quad K := \frac{k_{\max} - k_{\min}}{2}.$$

For every fixed $\hat{x} \in \mathbb{S}^2$, we define the far-field operator by

$$\begin{aligned} (F\phi)(\tau) &= (F^{(\hat{x})}\phi)(\tau) := \int_0^K w^\infty(\hat{x}, k_c + \tau - s) \phi(s) ds \\ &= \int_0^K \phi(s) \int_D e^{-i(k_c + \tau - s)\hat{x} \cdot y} f(y, k_c + \tau - s) dy ds. \end{aligned} \quad (2.10)$$

Since $w^\infty(\hat{x}, k)$ is analytic with respect to the wave number $k \in \mathbb{R}$, the operator $F^{(\hat{x})} : L^2(0, K) \rightarrow L^2(0, K)$ is bounded. For notational convenience we introduce the space

$$X_D := L^2(D \times (t_{\min}, t_{\max})).$$

Denote by $\langle \cdot, \cdot \rangle_{X_D}$ the inner product over X_D . Below we shall prove a factorization of the far-field operator.

Theorem 2.1. *We have $F = \sqrt{2\pi} L\mathcal{T}L^*$, where $L = L^{(\hat{x})} : X_D \rightarrow L^2(0, K)$ is defined by*

$$(Lu)(\tau) = \int_{t_{\min}}^{t_{\max}} \int_D e^{-i\tau(\hat{x} \cdot y + t)} u(y, t) dy dt, \quad \tau \in (0, K) \quad (2.11)$$

for all $u \in X_D$, and $\mathcal{T} : X_D \rightarrow X_D$ is a multiplication operator defined by

$$(\mathcal{T}u)(y, t) := e^{-ik_c(\hat{x} \cdot y + t)} S(y, t) u(y, t). \quad (2.12)$$

Proof. We first claim that the adjoint operator $L^* : L^2(0, K) \rightarrow X_D$ of L can be expressed by

$$(L^*\phi)(y, t) := \int_0^K e^{i\tau(\hat{x} \cdot y + t)} \phi(\tau) d\tau, \quad \phi \in L^2(0, K). \quad (2.13)$$

Indeed, for $u \in X_D$ and $\phi \in L^2(0, K)$, it holds that

$$\begin{aligned} \langle Lu, \phi \rangle_{L^2(0, K)} &= \int_0^K \left(\int_{t_{\min}}^{t_{\max}} \int_D e^{-i\tau(\hat{x} \cdot y + t)} u(y, t) dy dt \right) \overline{\phi(\tau)} d\tau \\ &= \int_{t_{\min}}^{t_{\max}} \int_D u(y, t) \left(\int_0^K \overline{\phi(\tau)} e^{i\tau(\hat{x} \cdot y + t)} d\tau \right) dy dt \\ &= \langle u, L^*\phi \rangle_{X_D} \end{aligned}$$

which implies (2.13). By the definition of \mathcal{T} ,

$$(\mathcal{T}L^*\phi)(y, t) = e^{-ik_c(\hat{x} \cdot y + t)} S(y, t) \int_0^K e^{is(\hat{x} \cdot y + t)} \phi(s) ds, \quad \phi \in L^2(0, K).$$

Hence, combining (1.5), (2.11) and (2.10) yields

$$\begin{aligned} (L\mathcal{T}L^*\phi)(\tau) &= \int_{t_{\min}}^{t_{\max}} \int_D e^{-i\tau(\hat{x} \cdot y + t)} \left(e^{-ik_c(\hat{x} \cdot y + t)} S(y, t) \int_0^K e^{is(\hat{x} \cdot y + t)} \phi(s) ds \right) dy dt \\ &= \int_0^K \int_D e^{-i(k_c + \tau - s)\hat{x} \cdot y} \phi(s) \left(\int_{t_{\min}}^{t_{\max}} S(y, t) e^{-i(k_c + \tau - s)t} dt \right) dy ds \\ &= \sqrt{2\pi} \int_0^K \int_D e^{-i(k_c + \tau - s)\hat{x} \cdot y} \phi(s) f(y, k_c + \tau - s) dy ds \\ &= \sqrt{2\pi} (F\phi)(\tau). \end{aligned}$$

This proves the factorization $F = \sqrt{2\pi} L\mathcal{T}L^*$. \square

The operator $L_D^{(\hat{x})}$ maps a time-dependent source function $S(x, t)$ supported on $\overline{D} \times (t_{\min}, t_{\max})$ to multi-frequency far-field patterns at the observation direction \hat{x} , that is, $w^\infty(\hat{x}, \cdot) = (L_D^{(\hat{x})} S)(\cdot)$. It will be referred to as the 'data-to-pattern' operator within this paper. Denote by $\text{Range}(L_D^{(\hat{x})})$ the range of the operator $L_D^{(\hat{x})}$ (see (2.11)) acting on X_D .

Lemma 2.1. *The operator $L_D^{(\hat{x})} : X_D \rightarrow L^2(0, K)$ is compact with dense range.*

Proof. For any $u \in X_D$, it holds that $L_D^{(\hat{x})} u \in H^1(0, K)$ by definition (2.11). Since $H^1(0, K)$ is compactly embedded into $L^2(0, K)$, we get the compactness of $L_D^{(\hat{x})}$. To prove the denseness of $\text{Range}(L_D^{(\hat{x})})$ in $L^2(0, K)$, we only need to prove the injectivity of $(L_D^{(\hat{x})})^*$. If $(L_D^{(\hat{x})})^* \phi = 0$ for some $\phi \in L^2(0, K)$, from (2.13) it follows that

$$\int_0^K e^{i\tau(\hat{x} \cdot y + t)} \phi(\tau) d\tau = 0 \quad \text{in } X_D.$$

Denote by $\tilde{\phi}$ the extension of ϕ by zero from $(0, K)$ to \mathbb{R} . The previous relation implies

$$0 = \frac{1}{\sqrt{2\pi}} \int_{\mathbb{R}} e^{i\tau(\hat{x} \cdot y + t)} \tilde{\phi}(\tau) d\tau = (\mathcal{F}^{-1} \tilde{\phi})(\xi)$$

where $\xi = \hat{x} \cdot y + t \in (\inf(\hat{x} \cdot D) + t_{\min}, \sup(\hat{x} \cdot D) + t_{\max})$. The analyticity of $(\mathcal{F}^{-1} \tilde{\phi})(\xi)$ in $\xi \in \mathbb{R}$ yields the identically vanishing of the inverse Fourier transform of $\tilde{\phi}$. This proves $\phi = 0$ and thus the injectivity of $(L_D^{(\hat{x})})^*$. \square

Now we want to connect the ranges of F and L . The existing range identities (see e.g., [29, Theorem 2.15] and [33, Theorems 4.1 and 4.4]) are not applicable to our case, because the real part of the middle operator \mathcal{T} (see (2.12)) cannot be decomposed into the sum of a positive and a compact operator. Nevertheless, the multiplication form of the middle operator motivates us to establish a new range identity. We first recall that, for a bounded operator $F : Y \rightarrow Y$ in a Hilbert space Y its real and imaginary parts are defined respectively by

$$\text{Re } F = \frac{F + F^*}{2}, \quad \text{Im } F = \frac{F - F^*}{2i}, \quad (2.14)$$

which are both self-adjoint operators. Furthermore, by spectral representation we define the self-adjoint and positive operator $|\text{Re } F|$ as

$$|\text{Re } F| = \int_{\mathbb{R}} |\lambda| dE_\lambda, \quad \text{if } \text{Re } F = \int_{\mathbb{R}} \lambda dE_\lambda.$$

The self-adjoint and positive operator $|\text{Im } F|$ can be defined analogously. In this paper the operator $F_\#$ is defined as

$$F_\# := |\text{Re } F| + |\text{Im } F|.$$

Since $F_\#$ is self-adjoint and positive, its square root $F_\#^{1/2}$ is given by

$$F_\#^{1/2} := \int_{\mathbb{R}_+} \sqrt{\lambda} dE_\lambda, \quad \text{if } F_\# = \int_{\mathbb{R}_+} \lambda dE_\lambda.$$

We need the following auxiliary result from functional analysis.

Theorem 2.2. *Let X and Y be Hilbert spaces and let $F : Y \rightarrow Y$, $L : X \rightarrow Y$, and $\mathcal{T} : X \rightarrow X$ be bounded linear operators such that $F = L\mathcal{T}L^*$. We make the following assumptions*

- (i) *L is compact with dense range and thus L^* is compact and one-to-one.*
- (ii) *$\operatorname{Re} \mathcal{T}$ and $\operatorname{Im} \mathcal{T}$ are both one-to-one and the operator $\mathcal{T}_\# = |\operatorname{Re} \mathcal{T}| + |\operatorname{Im} \mathcal{T}| : X \rightarrow X$ is coercive, i.e., there exists $c > 0$ with*

$$\langle \mathcal{T}_\# \varphi, \varphi \rangle_X \geq c \|\varphi\|_X^2 \quad \text{for all } \varphi \in X.$$

Then the operator $F_\#$ is positive and the ranges of $F_\#^{1/2} : Y \rightarrow Y$ and $L : X \rightarrow Y$ coincide.

Proof. We first recall from Part A in the proof of [29, Theorem 2.15] that it is sufficient to assume that $L^* : Y \rightarrow X$ has dense range in X . If otherwise, we may replace X by the closed subspace $\overline{\operatorname{Range}(L^*)}$ by using the orthogonal projection from X onto $\overline{\operatorname{Range}(L^*)}$. Below we shall prove the decomposition $F_\# = L\mathcal{T}_\#L^*$. For this purpose we only need to show

$$|\operatorname{Re} F| = L |\operatorname{Re} \mathcal{T}| L^*, \quad |\operatorname{Im} F| = L |\operatorname{Im} \mathcal{T}| L^*. \quad (2.15)$$

It suffices to consider the real part of F , because the imaginary part can be treated similarly. Since $\operatorname{Re} F = L (\operatorname{Re} \mathcal{T}) L^*$ is self-adjoint, it has a complete orthonormal eigensystem $\{(\lambda_j, \psi_j) : j \in \mathbb{N}\}$. Hence, the space Y can be split into two closed orthogonal subspaces $Y = Y^- \oplus Y^+$ with

$$Y^- = \operatorname{span}\{\psi_j : \lambda_j \leq 0\}, \quad Y^+ = \operatorname{span}\{\psi_j : \lambda_j \geq 0\}.$$

It is obvious that $\langle (\operatorname{Re} F)\psi, \psi \rangle_Y$ is non-negative on Y^+ and non-positive on Y^- . Consequently, $\langle (\operatorname{Re} \mathcal{T})\phi, \phi \rangle_X$ is non-negative on $U^+ := \overline{L^*(Y^+)}$ and is non-positive on $U^- := \overline{L^*(Y^-)}$, because

$$\langle (\operatorname{Re} \mathcal{T})\phi, \phi \rangle_X = \langle (\operatorname{Re} \mathcal{T})L^*(\psi^\pm), L^*(\psi^\pm) \rangle_X = \langle (\operatorname{Re} F)(\psi^\pm), \psi^\pm \rangle_Y \begin{matrix} \leq \\ \geq \end{matrix} 0, \quad (2.16)$$

where $\phi = L^*(\psi^\pm)$ with $\psi^\pm \in Y^\pm$. This implies that

$$\langle (\operatorname{Re} \mathcal{T})\phi, \phi \rangle_X = 0, \quad \text{if } \phi \in U^+ \cap U^-. \quad (2.17)$$

For $\phi \in U^+ \cap U^-$, we have $\phi^\pm + t\phi \in U^\pm$ for all $\phi^\pm \in U^\pm$ and for all $t \in \mathbb{C}$. This together with the relation (2.17) leads to $\langle (\operatorname{Re} \mathcal{T})\phi, \phi^\pm \rangle_X = 0$; see the Part C in the proof of [29, Theorem 2.15]. From this we deduce that $(\operatorname{Re} \mathcal{T})\phi = 0$. Since $\operatorname{Re} \mathcal{T}$ is one-to-one, we thus obtain $\phi = 0$. In view of the denseness of the range of L^* , this proves the orthogonal decomposition $X = U^+ \oplus U^-$.

To proceed with the proof, we denote by P_Y^\pm the orthogonal projectors from Y onto Y^\pm . Since $\operatorname{Re} F$ is invariant on both Y^+ and Y^- , there holds

$$|\operatorname{Re} F| = (P^+ - P^-)(\operatorname{Re} F) = (\operatorname{Re} F)(P^+ - P^-) = L (\operatorname{Re} \mathcal{T}) L^* (P^+ - P^-). \quad (2.18)$$

Introduce the projectors $Q_U^\pm : X \rightarrow U^\pm$. It is then easy to conclude the relations

$$(\operatorname{Re} \mathcal{T}) L^* P_Y^\pm = (\operatorname{Re} \mathcal{T}) Q_U^\pm L^*.$$

Therefore, using (2.18) and (2.16),

$$|\operatorname{Re} F| = L (\operatorname{Re} \mathcal{T}) L^* (P_Y^+ - P_Y^-) = L [(\operatorname{Re} \mathcal{T})(Q_U^+ - Q_U^-)] L^* = L |\operatorname{Re} \mathcal{T}| L^*,$$

which proves the first relation in (2.15) and thus also the decomposition $F_{\#} = L \mathcal{T}_{\#} L^*$. By the second assumption (ii), we obtain the positivity of $F_{\#}$. By the coercivity of $\mathcal{T}_{\#}$, we can define the square root operator $\mathcal{T}_{\#}^{1/2}$, which is also coercive and self-adjoint. Thus, we have a decomposition of $F_{\#}$ in the form

$$F_{\#} = (L \mathcal{T}_{\#}^{1/2}) (L \mathcal{T}_{\#}^{1/2})^* = F_{\#}^{1/2} (F_{\#}^{1/2})^*.$$

Application of [29, Theorem 1.21] gives

$$\operatorname{Range} (F_{\#}^{1/2}) = \operatorname{Range} (L).$$

□

To apply Theorem 2.2 to our inverse problem, we set

$$F = F_D^{(\hat{x})}, \quad X = X_D, \quad Y = L^2(0, K)$$

and let \mathcal{T} be the multiplication operator of (2.12). Since the source function $S(x, t)$ is real valued, it follows from (2.12) that

$$\begin{aligned} (\operatorname{Re} \mathcal{T}) u &= \cos(k_c(\hat{x} \cdot y + t)) S(y, t) u(y, t), \\ (\operatorname{Im} \mathcal{T}) u &= \sin(k_c(\hat{x} \cdot y + t)) S(y, t) u(y, t), \end{aligned}$$

both of them are one-to-one operators from X_D onto X_D . The coercivity assumption on S yields the coercivity of $\mathcal{T}_{\#}$, that is,

$$\begin{aligned} \langle \mathcal{T}_{\#} u, u \rangle &= \int_{t_{\min}}^{t_{\max}} \int_D \left(|\cos(k_c(\hat{x} \cdot y + t))| + |\sin(k_c(\hat{x} \cdot y + t))| \right) S(y, t) |u(y, t)|^2 dy dt \\ &\geq \frac{\sqrt{2}}{2} \int_{t_{\min}}^{t_{\max}} \int_D S(y, t) |u(y, t)|^2 dy dt \\ &\geq \frac{\sqrt{2}}{2} c_0 \|u\|_{X_D}^2. \end{aligned}$$

As a consequence of Theorem 2.2, we obtain

$$\operatorname{Range} [(F_D^{(\hat{x})})_{\#}^{1/2}] = \operatorname{Range} (L_D^{(\hat{x})}) \quad \text{for all } \hat{x} \in \mathbb{S}^2. \quad (2.19)$$

Let $\chi(k) \in L^2(0, K)$ be some test function. Denote by $(\lambda_n^{(\hat{x})}, \psi_n^{(\hat{x})})$ an eigensystem of the positive and self-adjoint operator $(F_D^{(\hat{x})})_{\#}$, which is uniquely determined by the multi-frequency

far-field patterns $\{w^\infty(\hat{x}, k) : k \in (k_{\min}, k_{\max})\}$. Applying Picard's theorem and Theorem 2.2, we obtain

$$\chi \in \text{Range}(L_D^{(\hat{x})}) \quad \text{if and only if} \quad \sum_{n=1}^{\infty} \frac{|\langle \chi, \psi_n^{(\hat{x})} \rangle|^2}{|\lambda_n^{(\hat{x})}|} < \infty. \quad (2.20)$$

To establish the factorization method, we now need to choose a suitable class of test functions which usually rely on a sample variable in \mathbb{R}^3 . The inclusion relationship between the test function and $\text{Range}(L_D^{(\hat{x})})$ should be associated with the inclusion relationship between the corresponding sample variable and the region D .

Remark 2.1. *In the special case that $k_{\min} = 0$, we can also apply the range identity of [33, Theorem 4.1] to get (2.19). In fact, since $w^\infty(\hat{x}, -k) = \overline{w^\infty(\hat{x}, k)}$, we may extend the bandwidth from $(0, k_{\max})$ to $(-k_{\max}, k_{\max})$. Hence, one deduces from these new measurement data with $k_{\min} = -k_{\max}$ that $k_c = 0$ and $K = k_{\max}$. Consequently, the middle operator \mathcal{T} is self-adjoint, due to the multiplication form $\mathcal{T}u = Su$ for $u \in X_D$. This implies that $F_D^{(\hat{x})}$ is also self-adjoint. Moreover, $F_D^{(\hat{x})}$ and \mathcal{T} are both positive definite under the assumption (1.2) and thus $(F_D^{(\hat{x})})_{\#} = F_D^{(\hat{x})}$, $\mathcal{T}_{\#} = \mathcal{T}$. The range identity stated in Theorem 2.2 allows us to handle a more general class of wave-number bands, in particular an interval of wave-numbers bounded away from zero.*

3 Range of $L_D^{(\hat{x})}$ and test functions

In this section we choose a proper class of test functions to characterize the range of $L_D^{(\hat{x})}$. Throughout the paper we set $T := t_{\max} - t_{\min} > 0$.

Lemma 3.1. *Let $D_1, D_2 \subset \mathbb{R}^3$ be bounded domains such that $\hat{x} \cdot D_1 \cap \hat{x} \cdot D_2 = \emptyset$. Suppose one the following relations holds*

$$\inf(\hat{x} \cdot D_1) - \sup(\hat{x} \cdot D_2) > T, \quad \inf(\hat{x} \cdot D_2) - \sup(\hat{x} \cdot D_1) > T. \quad (3.21)$$

Then $\text{Range}(L_{D_1}^{(\hat{x})}) \cap \text{Range}(L_{D_2}^{(\hat{x})}) = \{0\}$, that is, the ranges of $L_{D_j}^{(\hat{x})}$ over X_{D_1} and X_{D_2} have trivial intersections.

Proof. Let $f_j \in X_{D_j}$ be such that $L_{D_1}^{(\hat{x})} f_1 = L_{D_2}^{(\hat{x})} f_2 := \mathcal{G}(\cdot, \hat{x})$. By the definition of $L_D^{(\hat{x})}$ (see (2.11)), the function

$$\tau \mapsto \mathcal{G}(\tau, \hat{x}) = \int_{t_{\min}}^{t_{\max}} \int_{D_1} e^{-i\tau(\hat{x} \cdot y + t)} f_1(y, t) dy dt = \int_{t_{\min}}^{t_{\max}} \int_{D_2} e^{-i\tau(\hat{x} \cdot y + t)} f_2(y, t) dy dt$$

belongs to $L^2(0, K)$. Since $\mathcal{G}(\cdot, \hat{x})$ is analytic, the previous relation is valid for all $\tau \in \mathbb{R}$. Extending f_j by zero from (t_{\min}, t_{\max}) to \mathbb{R} and letting $\xi = \hat{x} \cdot y + t$, we can rewrite the integrals over D_j as

$$\int_{D_j} e^{-i\tau(\hat{x} \cdot y + t)} f_j(y, t) dy = \int_{\mathbb{R}} e^{-i\tau\xi} \int_{\Gamma_j(\xi - t, \hat{x})} f_j(y, t) ds(y) d\xi$$

where $\Gamma_j(t, \hat{x}) \subset D_j$ is defined as

$$\Gamma_j(t, \hat{x}) := \{y \in D_j : \hat{x} \cdot y = t\} \subset \mathbb{R}^3, \quad t \in \mathbb{R}, \quad j = 1, 2.$$

This implies that the function $\mathcal{G}(\cdot, \hat{x})$ is equivalent to the Fourier transform:

$$\mathcal{G}(\tau, \hat{x}) = \int_{\mathbb{R}} e^{-i\tau\xi} g_j(\xi, \hat{x}) d\xi, \quad \tau \in \mathbb{R}, \quad (3.22)$$

with

$$g_j(\xi, \hat{x}) := \int_{t_{\min}}^{t_{\max}} \int_{\Gamma_j(\xi-t, \hat{x})} f_j(y, t) ds(y) dt = \int_{\xi-t_{\max}}^{\xi-t_{\min}} \int_{\Gamma_j(t, \hat{x})} f_j(y, \xi-t) ds(y) dt$$

for $j = 1, 2$. By the arbitrariness of $\tau \in \mathbb{R}$, we get from (3.22) that $g_1(\xi, \hat{x}) = g_2(\xi, \hat{x})$ for all $\xi \in \mathbb{R}$. On the other hand, observing that

$$\Gamma_j(t, \hat{x}) = \emptyset \quad \text{if } t > \sup(\hat{x} \cdot D_j) \quad \text{or} \quad t < \inf(\hat{x} \cdot D_j),$$

we have

$$g_j(\xi, \hat{x}) = 0 \quad \text{if } \xi - t_{\min} < \inf(\hat{x} \cdot D_j) \quad \text{or} \quad \xi - t_{\max} > \sup(\hat{x} \cdot D_j).$$

This implies

$$\text{supp } g_j(\cdot, \hat{x}) \subset \left(\inf(\hat{x} \cdot D_j) + t_{\min}, \sup(\hat{x} \cdot D_j) + t_{\max} \right), \quad j = 1, 2,$$

By the conditions in (3.21), it is clear that one of the following relations holds:

$$\begin{aligned} \inf(\hat{x} \cdot D_1) + t_{\min} &> \sup(\hat{x} \cdot D_2) + t_{\max}, \\ \inf(\hat{x} \cdot D_2) + t_{\min} &> \sup(\hat{x} \cdot D_1) + t_{\max}, \end{aligned}$$

leading to $g_1(\xi, \hat{x}) = g_2(\xi, \hat{x}) \equiv 0$ for all $\xi \in \mathbb{R}$ in any case. Recalling (3.22), we obtain $L_{D_1}^{(\hat{x})} f_1 = L_{D_2}^{(\hat{x})} f_2 \equiv 0$. \square

As a consequence of the proof of Lemma 3.1, we can get information on the supporting interval of the inverse Fourier transform of $L_D^{(\hat{x})} f$ for $f \in X_D$ as follows.

Corollary 3.1. *Let $D \subset \mathbb{R}^3$ be a bounded domain and $t_{\max} > t_{\min}$. Define*

$$\mathcal{G}(\tau, \hat{x}) := \int_{t_{\min}}^{t_{\max}} \int_D e^{-i\tau(\hat{x} \cdot y + t)} f(y, t) dy dt, \quad f \in X_D.$$

Then the support of the inverse Fourier transform of $\mathcal{G}(\cdot, \hat{x})$ is contained in the interval $(\inf(\hat{x} \cdot D) + t_{\min}, \sup(\hat{x} \cdot D) + t_{\max})$.

For any $y \in \mathbb{R}^3$ and $\epsilon > 0$, define the test function $\phi_{y,\epsilon}^{(\hat{x})} \in L^2(0, K)$ by

$$\phi_{y,\epsilon}^{(\hat{x})}(k) = \frac{1}{T |B_\epsilon(y)|} \int_{t_{\min}}^{t_{\max}} \int_{B_\epsilon(y)} e^{-ik(\hat{x}\cdot z+t)} dz dt, \quad k \in (0, K). \quad (3.23)$$

where $|B_\epsilon(y)| = 4/3\pi\epsilon^3$ denotes the volume of the ball $B_\epsilon(y) \subset \mathbb{R}^3$. As $\epsilon \rightarrow 0$, there holds the convergence

$$\phi_{y,\epsilon}^{(\hat{x})}(k) \rightarrow \phi_y^{(\hat{x})}(k) := \frac{1}{T} \left(\int_{t_{\min}}^{t_{\max}} e^{-ikt} dt \right) e^{-ik\hat{x}\cdot y} = \frac{i}{kT} \left(e^{-ikt_{\max}} - e^{-ikt_{\min}} \right) e^{-ik\hat{x}\cdot y}. \quad (3.24)$$

Below we describe the supporting interval of the inverse Fourier transform of the test functions defined by (3.23).

Lemma 3.2. *For $\epsilon > 0$, we have*

$$[\mathcal{F}^{-1}\phi_{y,\epsilon}^{(\hat{x})}](\xi) > 0 \quad \text{if } \xi \in (\hat{x} \cdot y - \epsilon + t_{\min}, \hat{x} \cdot y + \epsilon + t_{\max}), \quad (3.25)$$

$$[\mathcal{F}^{-1}\phi_{y,\epsilon}^{(\hat{x})}](\xi) = 0 \quad \text{if } \xi \notin (\hat{x} \cdot y - \epsilon + t_{\min}, \hat{x} \cdot y + \epsilon + t_{\max}). \quad (3.26)$$

If $\epsilon = 0$, it holds that

$$[\mathcal{F}^{-1}\phi_y^{(\hat{x})}](\xi) = \begin{cases} \sqrt{2\pi}/T & \text{if } \xi \in (\hat{x} \cdot y + t_{\min}, \hat{x} \cdot y + t_{\max}), \\ 0 & \text{if otherwise.} \end{cases} \quad (3.27)$$

Proof. As done in (3.22), we can rewrite the function $\phi_{y,\epsilon}^{(\hat{x})}$ as

$$\phi_{y,\epsilon}^{(\hat{x})}(\tau) = \int_{\mathbb{R}} e^{-i\tau\xi} g_\epsilon(\xi, \hat{x}) d\xi, \quad g_\epsilon(\xi, \hat{x}) = \frac{1}{T} \int_{\xi-t_{\max}}^{\xi-t_{\min}} \int_{\Gamma(t,\hat{x})} ds(z) dt,$$

with $\Gamma(t, \hat{x}) = \{z \in B_\epsilon(y) : \hat{x} \cdot z = t\}$. Hence, $\mathcal{F}^{-1}\phi_{y,\epsilon}^{(\hat{x})} = \sqrt{2\pi} g_\epsilon(\cdot, \hat{x})$. Observing that

$$\sup(\hat{x} \cdot B_\epsilon(y)) = \hat{x} \cdot y + \epsilon, \quad \inf(\hat{x} \cdot B_\epsilon(y)) = \hat{x} \cdot y - \epsilon,$$

we obtain (3.25) and (3.26) from the expression of $g(\cdot, \hat{x})$. If $\epsilon = 0$, there holds

$$\phi_y^{(\hat{x})}(k) = \frac{1}{T} \int_{t_{\min}}^{t_{\max}} e^{-ik(t+\hat{x}\cdot y)} dt = \frac{1}{T} \int_{\mathbb{R}} e^{-ik\xi} g(\xi) d\xi,$$

where

$$g(\xi) := \begin{cases} 1 & \text{if } \xi \in (\hat{x} \cdot y + t_{\min}, \hat{x} \cdot y + t_{\max}). \\ 0 & \text{if otherwise.} \end{cases}$$

Therefore, $[\mathcal{F}^{-1}\phi_y^{(\hat{x})}](\xi) = \sqrt{2\pi} g(\xi)/T$. □

Introduce the strip (see Figure 1)

$$K_D^{(\hat{x})} := \{y \in \mathbb{R}^3 : \inf(\hat{x} \cdot D) < \hat{x} \cdot y < \sup(\hat{x} \cdot D)\} \subset \mathbb{R}^3. \quad (3.28)$$

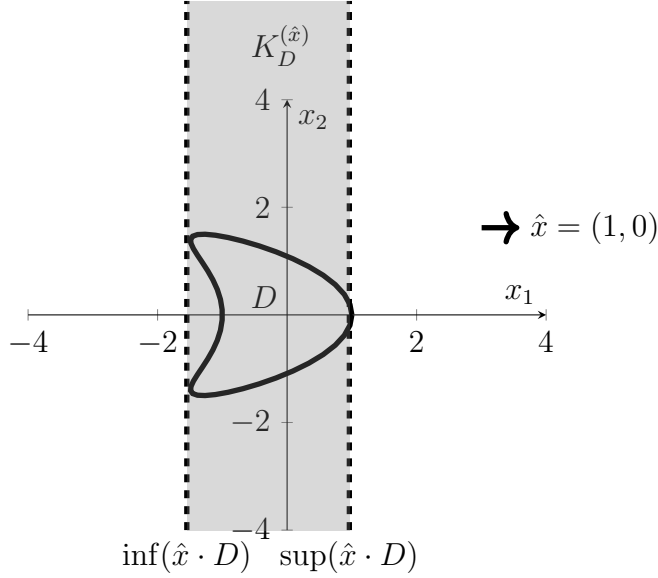


Figure 1: Illustration of the strip $K_D^{(\hat{x})}$ with $\hat{x} = (1, 0)$.

The set $K_D^{(\hat{x})} \subset \mathbb{R}^3$ represents the smallest strip containing D and perpendicular to the vector $\hat{x} \in \mathbb{S}^2$. We shall establish a computational criterion for imaging $K_D^{(\hat{x})}$ from the multi-frequency far-field data $u^\infty(\hat{x}, k)$ with $k \in (k_{\min}, k_{\max})$.

Lemma 3.3. (i) For $y \in K_D^{(\hat{x})}$, there exists $\epsilon_0 > 0$ such that $\phi_{y,\epsilon}^{(\hat{x})} \in \text{Range}(L_D^{(\hat{x})})$ for all $\epsilon \in (0, \epsilon_0)$.

(ii) If $y \notin K_D^{(\hat{x})}$, we have $\phi_{y,\epsilon}^{(\hat{x})} \notin \text{Range}(L_D^{(\hat{x})})$ for all $\epsilon > 0$.

Proof. (i) If $\hat{x} \cdot y \in \hat{x} \cdot D$, there must exist some $z \in D$ and $\epsilon_0 > 0$ such that $\hat{x} \cdot y = \hat{x} \cdot z$ and $B_\epsilon(z) \subset D$ for all $\epsilon \in (0, \epsilon_0)$. Moreover, we have $\phi_{y,\epsilon}^{(\hat{x})} = \phi_{z,\epsilon}^{(\hat{x})}$. Setting

$$u(x, t) := \begin{cases} \frac{1}{|B_\epsilon(z)|T}, & \text{if } x \in B_\epsilon(z), t \in (t_{\min}, t_{\max}), \\ 0 & \text{if otherwise.} \end{cases}$$

It is obvious that $u(x, t) \in L^2(D \times (t_{\min}, t_{\max}))$. By the definition of $L_D^{(\hat{x})}$ (see (2.11)), it is easy to see $\phi_{z,\epsilon}^{(\hat{x})} = L_D^{(\hat{x})}u$.

(ii) Given $y \notin K_D^{(\hat{x})}$, we suppose on the contrary that $\phi_{y,\epsilon}^{(\hat{x})} = L_D^{(\hat{x})}f$ with some $f \in L^2(D \times (t_{\min}, t_{\max}))$, i.e.,

$$\phi_{y,\epsilon}^{(\hat{x})}(\tau) = \int_{t_{\min}}^{\tau} \int_D e^{-i\tau(\hat{x} \cdot z + t)} f(z, t) dz dt, \quad \tau \in (0, K). \quad (3.29)$$

By the analyticity in τ , the above relation remains valid for all $\tau \in \mathbb{R}$. Hence, the supporting intervals of the inverse Fourier transform of both sides of (3.29) must coincide. Using (3.25) and Corollary 3.1, we obtain

$$(\hat{x} \cdot y - \epsilon + t_{\min}, \hat{x} \cdot y + \epsilon + t_{\max}) \subset (\inf(\hat{x} \cdot D) + t_{\min}, \sup(\hat{x} \cdot D) + t_{\max}),$$

leading to

$$\inf(\hat{x} \cdot D) + \epsilon \leq \hat{x} \cdot y \leq \sup(\hat{x} \cdot D) - \epsilon, \quad \text{for all } \epsilon > 0. \quad (3.30)$$

This implies that $y \in K_D^{(\hat{x})}$, a contradiction to the assumption $y \notin K_D^{(\hat{x})}$. This proves $\phi_{y,\epsilon}^{(\hat{x})} \notin \text{Range}(L_D^{(\hat{x})})$ for all $\epsilon > 0$. □

4 Indicator functions with multi-frequency far/near-field data

By Lemma 3.3, the functions $\phi_{y,\epsilon}^{(\hat{x})}$ with a small $\epsilon > 0$ can be taken as test functions to characterize D through (2.20). We first consider the indicator function involving $\phi_{y,\epsilon}^{(\hat{x})}$:

$$W_\epsilon^{(\hat{x})}(y) := \left[\sum_{n=1}^{\infty} \frac{|\langle \phi_{y,\epsilon}^{(\hat{x})}, \psi_n^{(\hat{x})} \rangle|_{L^2(0,K)}^2}{|\lambda_n^{(\hat{x})}|} \right]^{-1}, \quad y \in \mathbb{R}^3. \quad (4.31)$$

The analogue of (4.31) was used in [13] for imaging the support of a wave-number-independent source function. Combining Theorem 2.2 and Lemma 3.3 yields

Theorem 4.1. (i) *If $y \in K_D^{(\hat{x})}$, there exists $\epsilon_0 > 0$ such that $W_\epsilon^{(\hat{x})}(y) > 0$ for all $\epsilon \in (0, \epsilon_0)$.*

(ii) *If $y \notin K_D^{(\hat{x})}$ there holds $W_\epsilon^{(\hat{x})}(y) = 0$ for all $\epsilon > 0$.*

Since $\phi_{y,\epsilon}^{(\hat{x})}$ converges uniformly to $\phi_y^{(\hat{x})}$ over the finite wavenumber interval $[k_{\min}, k_{\max}]$, we shall use the limiting function $\phi_y^{(\hat{x})}$ in place of $\phi_{y,\epsilon}^{(\hat{x})}$ in the aforementioned indicator function. Consequently, we introduce a new indicator function

$$W^{(\hat{x})}(y) := \left[\sum_{n=1}^{\infty} \frac{|\langle \phi_y^{(\hat{x})}, \psi_n^{(\hat{x})} \rangle|_{L^2(0,K)}^2}{|\lambda_n^{(\hat{x})}|} \right]^{-1} \sim \left[\sum_{n=1}^N \frac{|\langle \phi_y^{(\hat{x})}, \psi_n^{(\hat{x})} \rangle|_{L^2(0,K)}^2}{|\lambda_n^{(\hat{x})}|} \right]^{-1}, \quad y \in \mathbb{R}^3, \quad (4.32)$$

where the integer $N \in \mathbb{N}$ is a truncation number. Taking the limit $\epsilon \rightarrow 0$ in Theorem 4.1, it follows that

$$W^{(\hat{x})}(y) = \begin{cases} \geq 0 & \text{if } y \in K_D^{(\hat{x})}, \\ 0 & \text{if } y \notin K_D^{(\hat{x})}. \end{cases} \quad (4.33)$$

Hence, the values of $W(\hat{x})$ in the strip $K_D^{(\hat{x})}$ should be relatively bigger than those elsewhere. In the case of sparse observation directions $\{\hat{x}_j : j = 1, 2, \dots, M\}$, we shall make use of the following indicator function:

$$W(y) = \left[\sum_{j=1}^M \frac{1}{W^{(\hat{x}_j)}(y)} \right]^{-1} = \left[\sum_{j=1}^M \sum_{n=1}^N \frac{|\langle \phi_y^{(\hat{x}_j)}, \psi_n^{(\hat{x}_j)} \rangle|_{L^2(0,K)}^2}{|\lambda_n^{(\hat{x}_j)}|} \right]^{-1}, \quad y \in \mathbb{R}^3. \quad (4.34)$$

Define the Θ -convex hull of D associated with the directions $\{\hat{x}_j : j = 1, 2, \dots, M\}$ as

$$\Theta_D := \bigcap_{j=1,2,\dots,M} K_D^{(\hat{x}_j)}.$$

Theorem 4.2. *We have $W(y) > 0$ if $y \in \Theta_D$ and $W(y) = 0$ if $y \notin \Theta_D$.*

Proof. If $y \in \Theta_D$, then $y \in K_D^{(\hat{x}_j)}$ for all $j = 1, 2, \dots, M$, yielding that $\hat{x}_j \cdot y \in \hat{x}_j \cdot D$. Hence, one deduces from Theorem 4.1 that $0 \leq W^{(\hat{x}_j)}(y) < \infty$ for all $j = 1, 2, \dots, M$, implying that $0 < W(y)$. On the other hand, if $y \notin \Theta_D$, there must exist some unit vector \hat{x}_l such that $y \notin K_D^{(\hat{x}_l)}$. Again, using Theorem 4.1 we get

$$[W^{(\hat{x}_l)}(y)]^{-1} = \sum_{n=1}^{\infty} \frac{|\langle \phi_y^{(\hat{x}_l)}, \psi_n^{(\hat{x}_l)} \rangle|_{L^2(0,K)}^2}{|\lambda_n^{(\hat{x}_l)}|} = \infty,$$

which proves $W(y) = 0$ for $y \notin \Theta_D$. \square

The values of $W(y)$ are expected to be large for $y \in \Theta_D$ and small for those $y \notin \Theta_D$. Below we shall provide a physical interpretation of the proposed inversion algorithm and build up connections with the time-dependent inverse source problems. We first remark that, the above factorization method with multi-frequency data carries over to near-field measurements in three dimensions. More precisely, the proposed factorization method can be slightly modified to get an image of the annular region

$$\tilde{K}_D^{(x)} := \{y \in \mathbb{R}^3 : \inf_{z \in D} |x - z| < |x - y| < \sup_{z \in D} |x - z|\} \subset \mathbb{R}^3 \quad (4.35)$$

for every fixed measurement position $|x| = R$. For this purpose we suppose $D \subset B_R$ for some $R > 0$ and define the near-field operator $\mathcal{N}^{(x)} : L^2(0, K) \rightarrow L^2(0, K)$ by

$$\begin{aligned} (\mathcal{N}^{(x)}\phi)(\tau) &:= \int_0^K w(x, k_c + \tau - s) \phi(s) ds \\ &= \int_0^K \int_D \frac{e^{i(k_c + \tau - s)|x - y|}}{4\pi|x - y|} f(y, k_c + \tau - s) dy \phi(s) ds \\ &= \int_0^K \int_D \frac{e^{i(k_c + \tau - s)|x - y|}}{4\pi|x - y|} \left(\int_{t_{\min}}^{t_{\max}} S(y, t) e^{-i(k_c + \tau - s)t} dt \right) dy \phi(s) ds \end{aligned} \quad (4.36)$$

where $x \in \partial B_R$ is a measurement position and $w \in H^2(B_R)$ is the solution to the Helmholtz equation (1.6). Following the proof of Theorem 2.1, we obtain a factorization of the near-field operator as follows:

$$\mathcal{N}^{(x)} = \tilde{L}\tilde{T}\tilde{L}^*.$$

where $\tilde{L} = \tilde{L}_D^{(x)} : X_D \rightarrow L^2(0, K)$ is defined by

$$(\tilde{L}u)(\tau) = \int_{t_{\min}}^{t_{\max}} \int_D e^{-i\tau(t-|x-y|)} u(y, t) dy dt, \quad \tau \in (0, K)$$

for all $u \in X_D$, and the middle operator $\tilde{T} : X_D \rightarrow X_D$ is again a coercive multiplication operator defined by

$$(\tilde{T}u)(y, t) := \frac{e^{-ik_\epsilon(t-|x-y|)}}{4\pi|x-y|} u(y, t) S(y, t), \quad |x| = R.$$

Note the the adjoint of $\tilde{L} : L^2(0, K) \rightarrow X_D$ is defined by

$$(\tilde{L}^*\phi)(y, t) := \int_0^K e^{is(t-|x-y|)} \phi(s) ds \in X_D, \quad \phi \in L^2(0, K).$$

Choose the test functions

$$\tilde{\phi}_{y,\epsilon}^{(x)}(k) := \frac{1}{T|B_\epsilon(y)|} \int_{t_{\min}}^{t_{\max}} \int_{B_\epsilon(y)} \frac{e^{ik(|x-z|-t)}}{4\pi|x-z|} dz dt,$$

which tends uniformly to

$$\tilde{\phi}_y^{(x)}(k) := \frac{i e^{ik|x-y|}}{4\pi k|x-y|T} \left(e^{-ikt_{\max}} - e^{-ikt_{\min}} \right),$$

as $\epsilon \rightarrow 0$ for all $k \in [k_{\min}, k_{\max}]$. Introduce the indicator function

$$\tilde{W}^{(x)}(y) := \left[\sum_{n=1}^{\infty} \frac{|\langle \tilde{\phi}_y^{(x)}, \tilde{\psi}_n^{(x)} \rangle|_{L^2(0,K)}^2}{|\lambda_n^{(x)}|} \right]^{-1}, \quad y \in \mathbb{R}^3, \quad (4.37)$$

where $(\tilde{\lambda}_n^{(x)}, \tilde{\psi}_n^{(x)})$ is an eigensystem of the near-field operator $(\mathcal{N}^{(x)})_{\#}$. As the counterpart to (4.34), one can show in the near-field case that

Corollary 4.1. (i) $Range[(\mathcal{N}^{(x)})_{\#}^{1/2}] = Range(\tilde{L}^{(x)})$ for all $x \in \partial B_R$.

(ii) It holds that

$$\tilde{W}^{(x)}(y) = \begin{cases} \geq 0 & \text{if } y \in \tilde{K}_D^{(x)}, \\ 0 & \text{if } y \notin \tilde{K}_D^{(x)}. \end{cases}$$

Now we want to bridge this near-field indicator functional with the time-domain signals of wave equations. In the near-field case, we suppose that the sparse data are given by $\{w(x_j, k) : x_j \in \partial B_R, k \in (k_{\min}, k_{\max})\}$, which can be considered as the Fourier transform of the time-dependent data $\{U(x_j, t) : x_j \in \partial B_R, t \in (0, T)\}$ for some $T > 2R + t_{\max}$. The time-dependent signals $t \mapsto U(x, t)$ with a fixed $x \in \partial B_R$ has a compact support, because the source term is compactly supported in $D \times (t_{\min}, t_{\max})$. Physically, this can be explained by the Huygens principle in 3D. Since the wave speed has been normalized to be one, it is not difficult to observe that the arrival time point T_{arr} and the terminal time point T_{ter} of the signal recorded by the sensor at $|x| = R$ are (see Figure 2)

$$T_{arr} = t_{\min} + \inf_{z \in D} |x - z|, \quad T_{ter} = t_{\max} + \sup_{z \in D} |x - z|,$$

respectively, where (t_{\min}, t_{\max}) represents the duration period for source radiating. This explains why the minimum distance and maximum distance between a measurement position x and our target D (which are equivalent to the annulus $\tilde{K}_D^{(x)}$) can be recovered from the multi-frequency near-field data at $|x| = R$.

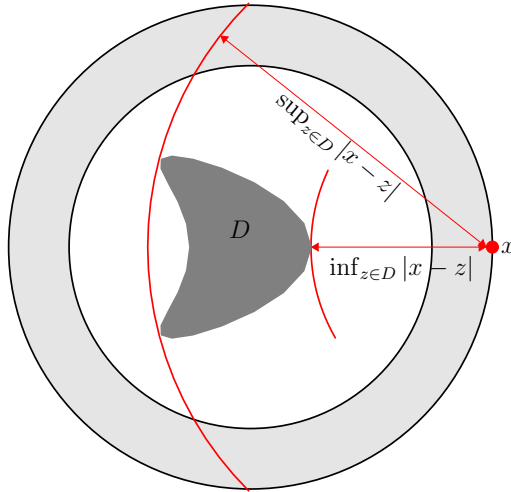


Figure 2: Illustration of the minimum and maximum distance between x and D . The annular domain represents the support of propagating waves. The region between the two red arcs forms $\tilde{K}_D^{(x)}$.

Remark 4.1. *The time window (t_{\min}, t_{\max}) is supposed to be a priori known in our inverse problem. A source term independent of wave-numbers corresponds to the critical case that $t_{\min} = t_{\max} = 0$ and $S(x, t) = f(x)\delta(t)$. In this special case, the test functions $\phi_{y, \epsilon}^{(\hat{x})}$ and $\phi_y^{(\hat{x})}$ are degenerated into*

$$\phi_{y, \epsilon}^{(\hat{x})}(k) = \frac{1}{|B_\epsilon(y)|} \int_{B_\epsilon(y)} e^{-ik\hat{x}\cdot z} dz, \quad \phi_y^{(\hat{x})}(k) = e^{-ik\hat{x}\cdot y}, \quad k \in (k_{\min}, k_{\max}).$$

which were used in [13] for recovering frequency-independent source terms.

As a by-product of the above factorization method, we obtain an uniqueness result with multi-frequency far-field data. Denote by $\text{ch}(D)$ the convex hull of D , that is, the intersections of all half spaces containing D .

Theorem 4.1. *Let the assumption (1.2) hold. Then $\text{ch}(D)$ can be uniquely determined by the multi-frequency far-field patterns $\{w^\infty(\hat{x}, k) : k \in (k_{\min}, k_{\max}), \hat{x} \in \mathbb{S}^2\}$.*

5 Discussions on source functions with two disconnected supports

In this section we discuss the factorization method for imaging the support of a wave-number-dependent source term with two disconnected components. For simplicity we only consider the far-field measurement data at multi-frequencies. Suppose that $D = D_1 \cup D_2 \subset \mathbb{R}^3$ contains two disjoint sub-domains D_j ($j = 1, 2$) which can be separated by some plane. The indicator function (4.32) can be used to image the strip $K_D^{(\hat{x})}$ if the multi-frequency data are observed at the direction \hat{x} . With the data for all observation directions the convex hull of D can be recovered from the indicator (4.34). Physically, it would be more interesting to determine $\text{ch}(D_j)$ for each $j = 1, 2$, whose union is usually only a subset of $\text{ch}(D)$. Analogously to Lemma 3.3 and Theorem 4.1, we can prove the following results.

Corollary 5.1. *Let $\hat{x} \in \mathbb{S}^2$ be fixed.*

(i) *For $y \in K_{D_1}^{(\hat{x})} \cup K_{D_2}^{(\hat{x})}$, we have $\phi_{y,\epsilon}^{(\hat{x})} \in \text{Range}(L_D^{(\hat{x})})$ for all $\epsilon \in (0, \epsilon_0)$ with some $\epsilon_0 > 0$.*

(ii) *If $y \notin K_{D_1}^{(\hat{x})} \cup K_{D_2}^{(\hat{x})}$, we have $\phi_{y,\epsilon}^{(\hat{x})} \notin \text{Range}(L_D^{(\hat{x})})$ for all $\epsilon > 0$, provided one of the following conditions holds*

$$(a) \inf(\hat{x} \cdot D_2) - \sup(\hat{x} \cdot D_1) > T; \quad (b) \inf(\hat{x} \cdot D_1) - \sup(\hat{x} \cdot D_2) > T. \quad (5.38)$$

(iii) *Let the indicator function $W^{(\hat{x})}$ be defined by (2.20). Under one of the conditions in (5.38) it holds that*

$$W^{(\hat{x})}(y) = \begin{cases} \geq 0 & \text{if } y \in K_{D_1}^{(\hat{x})} \cup K_{D_2}^{(\hat{x})}, \\ 0 & \text{if } y \notin (K_{D_1}^{(\hat{x})} \cup K_{D_2}^{(\hat{x})}). \end{cases}$$

Note that the conditions in (5.38) imply that $(\hat{x} \cdot D_1) \cap (\hat{x} \cdot D_2) = \emptyset$. Furthermore, the inverse Fourier transform of $L_D^{(\hat{x})} f$ with $f \in X_D$ is supported in the following two disjoint intervals (see Lemma 5.1 below for a detailed proof)

$$\left(\inf(\hat{x} \cdot D_1) + t_{\min}, \sup(\hat{x} \cdot D_1) + t_{\max} \right) \cup \left(\inf(\hat{x} \cdot D_2) + t_{\min}, \sup(\hat{x} \cdot D_2) + t_{\max} \right).$$

For small $T > 0$, there exists at least one observation directions $\hat{x} \in \mathbb{S}^2$ such that the relations in (5.38) hold, because D_1 and D_2 can be separated by some plane according to our assumption. If

the conditions (5.38) hold for all observation directions $\hat{x} \in \mathbb{S}^2$, one can make use of the indicator function (4.34) to get an image of the set $\bigcap_{j=1,2,\dots,M} \{K_{D_1}^{(\hat{x}_j)} \cup K_{D_2}^{(\hat{x}_j)}\}$, which is usually larger than $\text{ch}(D_1) \cup \text{ch}(D_2)$. This means that our approach can only be used to recover partial information of $\text{ch}(D_j)$, when the source radiating period T is sufficiently small in comparison with the distance between D_1 and D_2 . The numerical experiments performed in Section 6 confirm the above theory; see Figures 8 and 9.

Physically, the conditions in (5.38) ensure that the time-dependent signals recorded at \hat{x} has two disconnected supports which correspond to the radiated wave fields from D_1 and D_2 , respectively. If one can split the multi-frequency far-field patterns at a single observation direction, it is still possible to recover $\{K_{D_1}^{(\hat{x})} \cup K_{D_2}^{(\hat{x})}\}$ even if the conditions in (5.38) cannot be fulfilled. Below we prove that the multi-frequency far-field patterns excited by two disconnected source terms can be split under additional assumptions.

To rigorously formulate the splitting problem, we go back to the wave equation (1.1), where $D = D_1 \cup D_2$ contains two disjoint bounded and connected sub-domains D_1 and D_2 . As seen in (1.3), the solution $U = G * S$ can be written explicitly as the convolution of the fundamental solution G with the source term S . Define $U_j := G * S_j$ with $S_j := S|_{D_j \times \mathbb{R}_+}$. It is obvious that $U(x, t) = U_1(x, t) + U_2(x, t)$ for $(x, t) \in \mathbb{R}^3 \times \mathbb{R}_+$. In the frequency domain, we consider the time-harmonic source problem

$$\Delta u + k^2 u = f_1(\cdot, k) + f_2(\cdot, k) \quad \text{in } \mathbb{R}^3 \times \mathbb{R}_+,$$

where $\text{supp} f_j(\cdot, k) = D_j$ for any $k > 0$ and

$$f_j(x, k) := \int_{t_{\min}}^{t_{\max}} S_j(x, t) e^{-ikt} dt, \quad x \in D_j.$$

Let u_j be the unique radiating solution to

$$\Delta u_j + k^2 u_j = f_j(x, k) \quad \text{in } \mathbb{R}^3 \times \mathbb{R}_+, \quad j = 1, 2.$$

Denote by $u^\infty(\hat{x}, k)$, $u_j^\infty(\hat{x}, k)$ the far-field patterns of u and u_j at some fixed observation direction $\hat{x} = x/|x|$, respectively. It is obvious that $u^\infty = u_1^\infty + u_2^\infty$, where

$$u_j^\infty(\hat{x}, k) = \int_{t_{\min}}^{t_{\max}} \int_{D_j} S_j(y, t) e^{-ik(\hat{x} \cdot y + t)} dy dt, \quad k \in \mathbb{R}_+. \quad (5.39)$$

The splitting problem in the frequency domain can be formulation as follows: Given a fixed observation direction $\hat{x} \in \mathbb{S}^2$, split $\{u_j^\infty(\hat{x}, k) : k \in \mathbb{R}\}$ from the data $\{u^\infty(\hat{x}, k) : k \in \mathbb{R}\}$ for $j = 1, 2$.

Set $l_j := \sup(\hat{x} \cdot D_j) - \inf(\hat{x} \cdot D_j)$ and $\Lambda_j = T + l_j$. We make the following assumptions on the time-dependent source function $S(x, t)$.

- (i) $S(x, t) \geq c_0 > 0$ for $(x, t) \in D \times (t_{\min}, t_{\max})$.

(ii) S is analytic on $\bar{D} \times [t_{\min}, t_{\max}]$ and the boundary ∂D is analytic.

(iii) Either $\inf(\hat{x} \cdot D_1) < \inf(\hat{x} \cdot D_2)$, or $\sup(\hat{x} \cdot D_1) > \sup(\hat{x} \cdot D_2)$.

Lemma 5.1. *Under the assumption (i), the supporting interval of $\mathcal{F}^{-1}[u_j^\infty(k, \hat{x})]$ is $I_j := (\inf(\hat{x} \cdot D_j) + t_{\min}, \sup(\hat{x} \cdot D_j) + t_{\max})$ and the function $t \mapsto (\mathcal{F}^{-1}u_j^\infty)(t)$ is positive in I_j . Moreover, $(\mathcal{F}^{-1}u_j^\infty)(t)$ is analytic in $t \in I_j$ under the additional assumption (ii).*

Proof. We carry out the proof following the ideas in the proof of Lemma 3.1. The far-field expression (5.39) can be rewritten as

$$u_j^\infty(\hat{x}, k) = \int_{\mathbb{R}} e^{-ik\xi} g_j(\xi) d\xi, \quad j = 1, 2,$$

where

$$g_j(\xi) := \int_{t_{\min}}^{t_{\max}} \int_{\Gamma_j(\xi-t)} S_j(y, t) ds(y) dt = \int_{\xi-t_{\max}}^{\xi-t_{\min}} \int_{\Gamma_j(t)} S_j(y, \xi-t) ds(y) dt. \quad (5.40)$$

Here $\Gamma_j(t) \subset D_j$ is defined as $\Gamma_j(t) := \{y \in D_j : \hat{x} \cdot y = t\}$. By the assumption (i) we deduce from (5.40) with $\xi = \inf(\hat{x} \cdot D_j) + t_{\min} + \epsilon$, $\epsilon \in (0, \Lambda_j)$ that

$$g_j(\xi) = \int_{\inf(\hat{x} \cdot D_j)}^{\inf(\hat{x} \cdot D_j) + \epsilon} \int_{\Gamma_j(t)} S_j(y, \xi-t) ds(y) dt > 0,$$

because

$$\begin{aligned} \xi - t &\in (t_{\min}, t_{\min} + \epsilon) && \text{if } t \in \left(\inf(\hat{x} \cdot D_j), \inf(\hat{x} \cdot D_j) + \epsilon \right), \\ \xi - t &\in \left(\inf(\hat{x} \cdot D_j) + \epsilon - T, \inf(\hat{x} \cdot D_j) + \epsilon \right) && \text{if } t \in (t_{\min}, t_{\max}). \end{aligned}$$

Since g_j coincides with the inverse Fourier transform of u_j^∞ by a factor, this proves the first part of the lemma. The analyticity of $(\mathcal{F}^{-1}u_j^\infty)(t)$ in $t \in I_j$ follows from (5.40) under the assumption (ii). \square

Next we show that the multi-frequency far-field measurement data at a fixed observation direction can be uniquely split. Note that the splitting is obvious under the conditions in (5.38), because by Lemma 5.1 the inverse Fourier transform of $u^\infty(\hat{x}, k)$ has two disconnected components.

Theorem 5.1. *Suppose that there are two time-dependent sources S and \tilde{S} with $\text{supp } \tilde{S} = \tilde{D} \times (t_{\min}, t_{\max})$ and $\tilde{D} = \tilde{D}_1 \cup \tilde{D}_2$. Here the source function \tilde{S} and its support \tilde{D} are also required to satisfy the assumptions (i)-(iii). Let \tilde{u}_j^∞ be defined by (5.39) with D_j, S_j replaced by $\tilde{D}_j, \tilde{S}_j := \tilde{S}|_{\tilde{D}_j \times (t_{\min}, t_{\max})}$, respectively. Then the relation*

$$u^\infty(\hat{x}, k) = u_1^\infty(\hat{x}, k) + u_2^\infty(\hat{x}, k) = \tilde{u}_1^\infty(\hat{x}, k) + \tilde{u}_2^\infty(\hat{x}, k), \quad k \in (k_{\min}, k_{\max}) \quad (5.41)$$

implies that $u_j^\infty(\hat{x}, k) = \tilde{u}_j^\infty(\hat{x}, k)$ for $k \in (k_{\min}, k_{\max})$ and $j = 1, 2$.

Proof. By the analyticity of $u_j^\infty, \tilde{u}_j^\infty$ in $k \in \mathbb{R}$, the function u^∞ can be analytically extended to the whole real axis. Denote by (T_{\min}, T_{\max}) the supporting interval of the inverse Fourier transform of u^∞ with respect to k . In view of assumption (iii) and Lemma 5.1, we may suppose without loss of generality that $T_{\min} = \Lambda_{\min} + t_{\min}$ with

$$\Lambda_{\min} = \inf(\hat{x} \cdot D_1) = \inf(\hat{x} \cdot \tilde{D}_1) < \inf(\hat{x} \cdot D_2), \quad \Lambda_{\min} < \inf(\hat{x} \cdot \tilde{D}_2).$$

If otherwise, there must hold $T_{\max} = \Lambda_{\max} + t_{\max}$ with

$$\Lambda_{\max} = \sup(\hat{x} \cdot D_1) = \sup(\hat{x} \cdot \tilde{D}_1) > \sup(\hat{x} \cdot D_2), \quad \Lambda_{\max} > \sup(\hat{x} \cdot \tilde{D}_2)$$

and the proof can be carried out similarly.

Define $w_j = u_j^\infty - \tilde{u}_j^\infty$ for $j = 1, 2$. Using (5.41), we get $w_1(\hat{x}, k) = w_2(\hat{x}, k)$ for all $k \in \mathbb{R}$. Hence, their inverse Fourier transforms must also coincide, i.e., $[\mathcal{F}^{-1}w_1](t) = [\mathcal{F}^{-1}w_2](t)$ for all $t \in \mathbb{R}$. Taking $\delta < \min\{\inf(\hat{x} \cdot D_2) - \Lambda_{\min}, \inf(\hat{x} \cdot \tilde{D}_2) - \Lambda_{\min}\}$. Again using Lemma 5.1, we obtain

$$0 = [\mathcal{F}^{-1}w_2](t) = [\mathcal{F}^{-1}w_1](t) \quad \text{for all } t \in (T_{\min}, T_{\min} + \delta)$$

because the interval $(T_{\min}, T_{\min} + \delta)$ lies in the exterior of the supporting intervals of both $\mathcal{F}^{-1}u_2^\infty$ and $\mathcal{F}^{-1}\tilde{u}_2^\infty$. Combining this with the analyticity of $[\mathcal{F}^{-1}w_1](t)$ in t , we get

$$[\mathcal{F}^{-1}w_1](t) = 0 \quad \text{for all } t \in \left(T_{\min}, \min\left\{\sup(\hat{x} \cdot D_1), \sup(\hat{x} \cdot \tilde{D}_1)\right\} + t_{\max}\right). \quad (5.42)$$

If $\sup(\hat{x} \cdot D_1) < \sup(\hat{x} \cdot \tilde{D}_1)$, it is seen from Lemma 5.1 that

$$[\mathcal{F}^{-1}u_1^\infty](t^*) = 0, \quad [\mathcal{F}^{-1}\tilde{u}_1^\infty](t^*) > 0 \quad (5.43)$$

where

$$t^* = \sup(\hat{x} \cdot D_1) + t_{\max} \in I_j = \left(\inf(\hat{x} \cdot \tilde{D}_1) + t_{\min}, \sup(\hat{x} \cdot \tilde{D}_1) + t_{\max}\right).$$

Obviously, the relations in (5.43) contradicts the fact that $[\mathcal{F}^{-1}w_1](t^*) = 0$ by (5.42). This proves $\sup(\hat{x} \cdot D_1) \geq \sup(\hat{x} \cdot \tilde{D}_1)$. The relation $\sup(\hat{x} \cdot D_1) \leq \sup(\hat{x} \cdot \tilde{D}_1)$ can be proved analogously. Hence, $\sup(\hat{x} \cdot D_1) = \sup(\hat{x} \cdot \tilde{D}_1) := \Lambda_{\max}$ and

$$[\mathcal{F}^{-1}w_1](t) = 0 \quad \text{for all } t \in \left(\Lambda_{\min} + t_{\min}, \Lambda_{\max} + t_{\max}\right).$$

Using again Lemma 5.1 we find that $\mathcal{F}^{-1}u_1^\infty$ and $\mathcal{F}^{-1}\tilde{u}_1^\infty$ also vanish for $t \notin (\Lambda_{\min} + t_{\min}, \Lambda_{\max} + t_{\max})$. Therefore, $w_1 \equiv 0$ and $u_1^\infty \equiv \tilde{u}_1^\infty$, which implies $u_2^\infty \equiv \tilde{u}_2^\infty$. \square

Remark 5.1. Once $u_j^\infty(\hat{x}, k)$ ($j = 1, 2$) can be computed from $u^\infty(\hat{x}, k)$, one can apply the factorization scheme proposed in Sections 2-4 to get an image of the strip $K_{D_j}^{(\hat{x})}$ for $j = 1, 2$. The numerical implementation of the multi-frequency far-field splitting at a single observation direction is beyond the scope of this paper. We refer to [18] for a numerical scheme for splitting far-field patterns over all directions at a fixed frequency.

6 Numerical examples

In this section, we present a couple of numerical examples in \mathbb{R}^2 to test the proposed factorization method with far-field measurements. All numerical examples are implemented by MATLAB. We first describe the reconstruction procedure with multi-frequency far-field data over a single or multiple observation directions. Unless otherwise stated, we always assume $k_{\min} = 0$. With such a choice the far-field operator (2.10) can be simplified to be

$$(F^{(\hat{x})}\phi)(\tau) = \int_0^{k_{\max}} w^\infty(\hat{x}, \tau - s)\phi(s)ds, \quad L^2(0, k_{\max}) \rightarrow L^2(0, k_{\max}) \quad (6.44)$$

by taking $k_c = 0$ and $K = k_{\max}$; see Remark 2.1. In our numerical examples below, we consider $2N - 1$ wave-number samples $w^\infty(\hat{x}, k_n), n = 1, 2, \dots, N$, and $w^\infty(\hat{x}, -k_n), n = 1, 2, \dots, N - 1$ of the far field, where

$$k_n = (n - 0.5)\Delta k, \quad \Delta k := \frac{k_{\max}}{N}.$$

Using the $2N - 1$ samples of the far field in (6.44) and applying the midpoint rule, we obtain from (6.44) that

$$(F^{(\hat{x})}\phi)(\tau_n) \approx \sum_{m=1}^N w^\infty(\hat{x}, \tau_n - s_m)\phi(s_m)\Delta k$$

where $\tau_n := n\Delta k$ and $s_m := (m - 0.5)\Delta k, n, m = 1, 2, \dots, N$. Accordingly, a discrete approximation of $F^{(\hat{x})}$ is given by the Toeplitz matrix

$$F^{(\hat{x})} := \begin{pmatrix} w^\infty(\hat{x}, k_1) & \overline{w^\infty(\hat{x}, k_1)} & \cdots & \overline{w^\infty(\hat{x}, k_{N-2})} & \overline{w^\infty(\hat{x}, k_{N-1})} \\ w^\infty(\hat{x}, k_2) & w^\infty(\hat{x}, k_1) & \cdots & \overline{w^\infty(\hat{x}, k_{N-3})} & \overline{w^\infty(\hat{x}, k_{N-2})} \\ \vdots & \vdots & & \vdots & \vdots \\ w^\infty(\hat{x}, k_{N-1}) & w^\infty(\hat{x}, k_{N-2}) & \cdots & w^\infty(\hat{x}, k_1) & \overline{w^\infty(\hat{x}, k_1)} \\ w^\infty(\hat{x}, k_N) & w^\infty(\hat{x}, k_{N-1}) & \cdots & w^\infty(\hat{x}, k_2) & w^\infty(\hat{x}, k_1) \end{pmatrix} \Delta k \quad (6.45)$$

where $\overline{w^\infty(\hat{x}, k_n)} = w^\infty(\hat{x}, -k_n), n = 1, \dots, N - 1$ and $F^{(\hat{x})}$ is a $N \times N$ complex matrix. For any point $y \in \mathbb{R}^2$ we define the test function vector $\phi_y^{(\hat{x})} \in \mathbb{C}^N$ from (3.24) by

$$\phi_y^{(\hat{x})} := \left(\frac{i}{T\tau_1} (e^{-i\tau_1 T} - 1) e^{-i\tau_1 \hat{x} \cdot y}, \dots, \frac{i}{T\tau_N} (e^{-i\tau_N T} - 1) e^{-i\tau_N \hat{x} \cdot y} \right), \quad (6.46)$$

where $T = t_{\max} - t_{\min}$. Denoting by $\{(\tilde{\lambda}_n^{(\hat{x})}, \psi_n^{(\hat{x})}) : n = 1, 2, \dots, N\}$ an eigen-system of the matrix $F^{(\hat{x})}$ (6.45), then one deduces that an eigen-system of the matrix $(F^{(\hat{x})})_\# := |\operatorname{Re}(F^{(\hat{x})})| + |\operatorname{Im}(F^{(\hat{x})})|$ is $\{(\lambda_n^{(\hat{x})}, \psi_n^{(\hat{x})}) : n = 1, 2, \dots, N\}$, where $\lambda_n^{(\hat{x})} := |\operatorname{Re}(\tilde{\lambda}_n^{(\hat{x})})| + |\operatorname{Im}(\tilde{\lambda}_n^{(\hat{x})})|$. We approximate the indicator function $W^{(\hat{x})}$ in (2.20) by

$$W^{(\hat{x})}(y) := \left[\sum_{n=1}^N \frac{|\phi_y^{(\hat{x})} \cdot \overline{\psi_n^{(\hat{x})}|^2}{|\lambda_n^{(\hat{x})}|} \right]^{-1}, \quad y \in \mathbb{R}^2,$$

where \cdot denotes the inner product in \mathbb{R}^N . Accordingly, a plot of $W^{(\hat{x})}(y)$, should yield a visualization of the strip $K_D^{(\hat{x})}$ (see (4.35)) containing the source support. In the following numerical examples, the frequency band is taken as $(0, 16\pi/6)$ with $k_{\max} = 16\pi/6$, $N = 16$ and $\Delta k = \pi/6$. The wave-number-dependent source term $f(x, k)$ is supposed to be given by (1.5). We always take $t_{\min} = 0$ and $t_{\max} = T = 0.1$ unless otherwise specified.

6.1 One observation direction

We first consider reconstruction of the strip $K_D^{(\hat{x})}$ from the multi-frequency far-field data $w^\infty(\hat{x}, \pm k_n)$. In Fig.3, we show a visualization of reconstructions of three sources supported on a kite-shaped domain at the observation direction $\hat{x} = (\cos \theta, \sin \theta)$ with the angle $\theta \in (0, 2\pi]$. The time-dependent source functions are chosen as $S(x, t)$ satisfying the coercivity assumption (1.2). We choose $S(x, t) = 3(t + 1)$ and $\theta = \pi/4$ in Fig.3 (a); $S(x, t) = 3x_1(t + 1)$ and $\theta = \pi/2$ in Fig.3 (b); $S(x, t) = 3(x_1^2 + x_2^2 - 4)(t + 1)$ and $\theta = 3\pi/4$ in Fig.3 (c). The boundary of D is also shown in the picture (pink-solid line). As predicted by our theoretical results, the reconstructions nicely approximate the smallest strip $K_D^{(\hat{x})}$ perpendicular to the observation directions that contains the support.

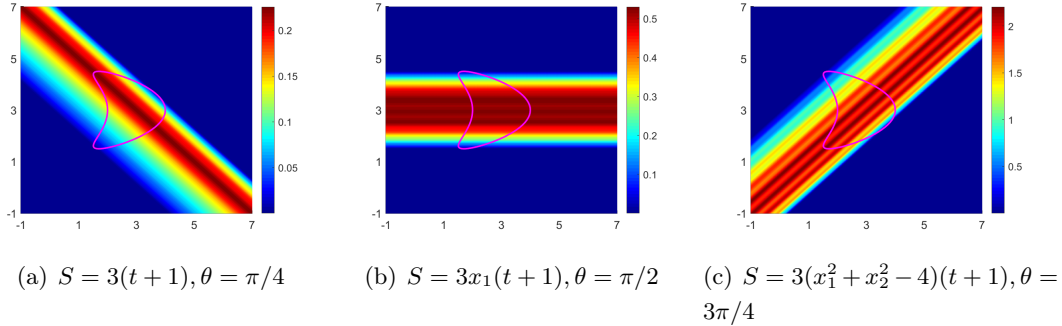


Figure 3: Reconstructions using a single observation direction and multi-frequency far-field data for a kite-shaped support. We choose $t_{\min} = 0$ and $t_{\max} = T = 0.1$.

Next, we continue the numerical example for $S(x, t) = 3(x_1^2 + x_2^2 - 4)(t + 1)$ and $\theta = 3\pi/4$ in Fig.3 (c) but with different Fourier transform windows (t_{\min}, t_{\max}) . We take $t_{\min} = 0, t_{\max} = T$ with $T = 1, 2, 3$ in Fig.4. The Fourier transform window is taken to be $(t_{\min}, t_{\max}) = (T_0, T_0 + T)$ in Fig. 5, with $T = 0.1$ and $T_0 = 1, 2, 3$. In the last case, the test vector (6.46) is discretized as

$$\phi_y^{(\hat{x})} := \left(\frac{i}{T\tau_1} (e^{-i\tau_1(T_0+T)} - e^{-i\tau_1 T_0}) e^{-i\tau_1 \hat{x} \cdot y}, \dots, \frac{i}{T\tau_n} (e^{-i\tau_n(T_0+T)} - e^{-i\tau_n T_0}) e^{-i\tau_n \hat{x} \cdot y} \right) \in \mathbb{C}^N.$$

It is clearly shown that the source still lies in the smallest strip perpendicular to the observation direction. The numerical examples in Figs 4 and 5 show that our inversion algorithm is independent of the choice of t_{\min} and t_{\max} .

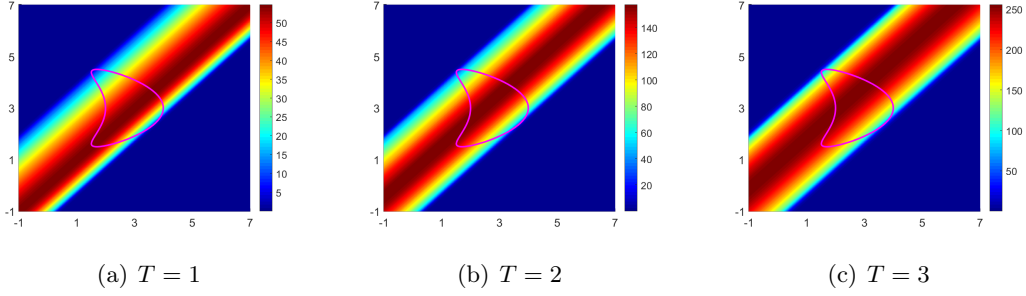


Figure 4: Reconstructions of a kite-shaped support with $S = 3(x_1^2 + x_2^2 - 4)(t + 1)$ and $\theta = 3\pi/4$ with different Fourier transform windows $(0, T)$.

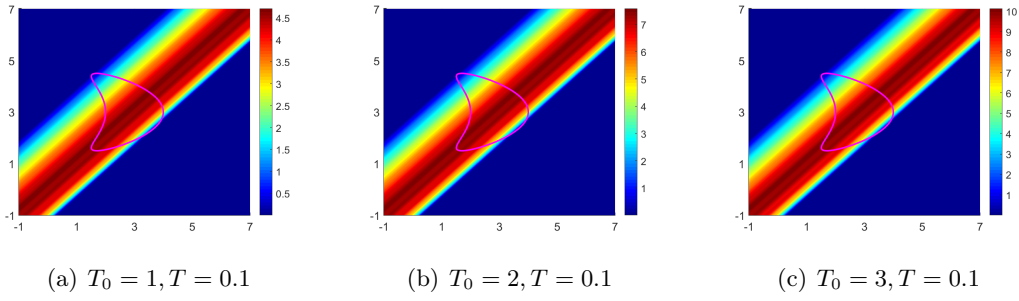


Figure 5: Reconstructions of a kite-shaped support with $S = 3(x_1^2 + x_2^2 - 4)(t + 1)$, $\theta = 3\pi/4$ and with different Fourier transform windows of the form $(T_0, T_0 + T)$.

6.2 Multiple observation directions

We present the reconstruction of a kite-shaped source using M observation directions with the observation angles $\theta_m = \frac{m-1}{M}\pi$, $m = 1, \dots, M$. Here, one should change the indicator function into

$$W^{(\hat{x})}(y) := \left[\sum_{m=1}^M \sum_{n=1}^N \frac{|\phi_y^{(\hat{x}_m)} \cdot \overline{\psi_n^{(\hat{x}_m)}}|^2}{|\lambda_n^{(\hat{x}_m)}|} \right]^{-1}, \quad y \in \mathbb{R}^2.$$

where the test function $\phi_y^{(\hat{x}_m)}$ is again given by (6.46), and $\{(\lambda_n^{(\hat{x}_m)}, \psi_n^{(\hat{x}_m)}) : n = 1, \dots, N\}$ denotes an eigensystem of the operator $(F^{(\hat{x}_m)})_{\#}$.

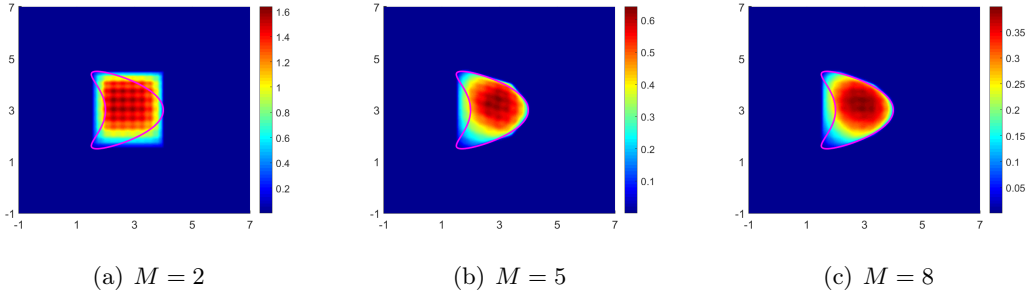


Figure 6: Reconstructions of a kite-shaped source for $S = 3(x_1^2 + x_2^2)(t + 1)$ with M observation directions. The Fourier transform window (t_{\min}, t_{\max}) is chosen as $t_{\min} = 0$ and $t_{\max} = 0.1$.

We show in Fig.6 a visualization of the reconstructed source with $S(x, t) = 3(x_1^2 + x_2^2)(t + 1)$. Since the observation directions are perpendicular to each other if $M = 2$, the strips $K_D^{(\hat{x}_1)}$ and $K_D^{(\hat{x}_2)}$ are also perpendicular to each other as shown in Fig.6 (a). It is clear that intersection of the strips contains the source support in Fig.6 (a), (b) and (c), which approximates the convex hull of the support. Of course the number of observation directions affects reconstruction qualities: the more the directions, the better the reconstructions.

We continue the numerical example in Fig.6 (c) by choosing different Fourier transform time windows $(0, T)$. The resulting reconstructions are shown in Fig. 7 with three different choices $T = 1, 5, 7$. The results are getting worse with increasing T , but they still contain useful information on the location and shape of the source. In other numerical examples, we all take $T = 0.1$ to get precise reconstructions.

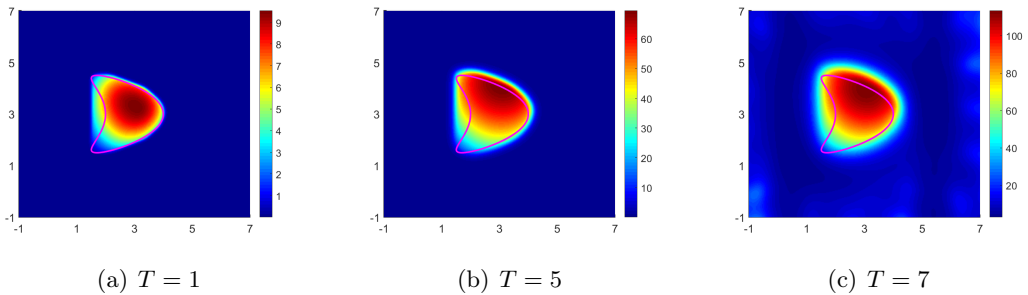


Figure 7: Reconstructions from $M = 8$ observation directions for a kite-shaped support. We choose $S = 3(x_1^2 + x_2^2)(t + 1)$ and different Fourier transform windows of the form $(0, T)$.

Next we consider a source with two disconnected components: one component is kite-shaped and the other one is elliptic. We choose different source functions in Fig.8. It is shown that the two components are both precisely recovered using 8 observation directions. It is worth mentioning that the Fourier transform time widow $(0, T)$ should not be too big in this case. If T is increasing from 1 to 5, the images will be distorted; see Fig.9. This is due to the reason that

the wave-fields radiated from the two components and received by the sensors cannot be split. The Fig.9 (b) can be improved if we increase the number of frequencies. However, if T is larger than the distance between the two components (see Fig.9 (c)), the two components cannot be well separated. Instead, the convex hull of the union of these two components can be recovered.

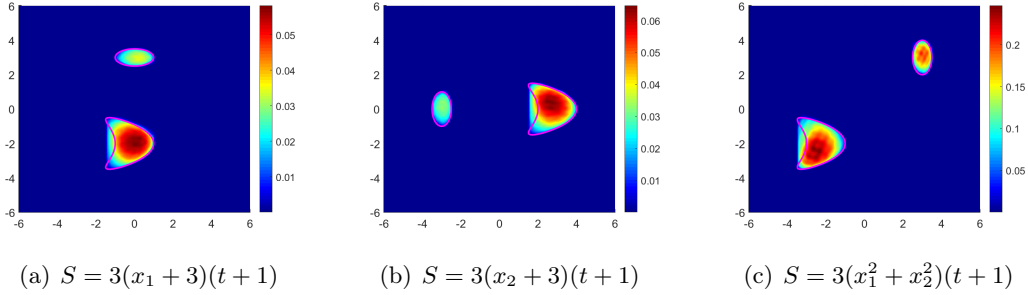


Figure 8: Reconstructions of the shape of a source with two components from 8 observation directions. The Fourier time window is $(0, T)$ with $T = 0.1$.

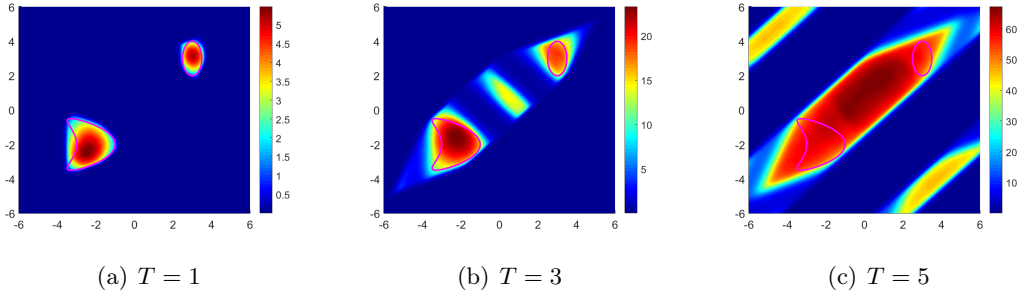


Figure 9: Reconstructions of two disjoint components from 8 observation directions with different time windows $(0, T)$. The source function is $S = 3(x_1^2 + x_2^2)(t + 1)$.

To test the sensitivity of the algorithm with respect to measurement noise, we pollute the far-field data matrix by

$$F_\delta^{(\hat{x})} := F^{(\hat{x})} + \delta \|F^{(\hat{x})}\|_2 \mathcal{M}$$

where δ is the noise level and $\mathcal{M} \in \mathbb{R}^{N \times N}$ is a uniformly distributed random -matrix with the random variable ranging from -1 to 1 . The resulting reconstructions are shown in Fig.10 at three noise levels. The images are clearly getting distorted at higher noise levels, but the location of the source can still be well-captured. Here we did not present the reconstruction in the noise-free case, since the other examples have shown the effectiveness.

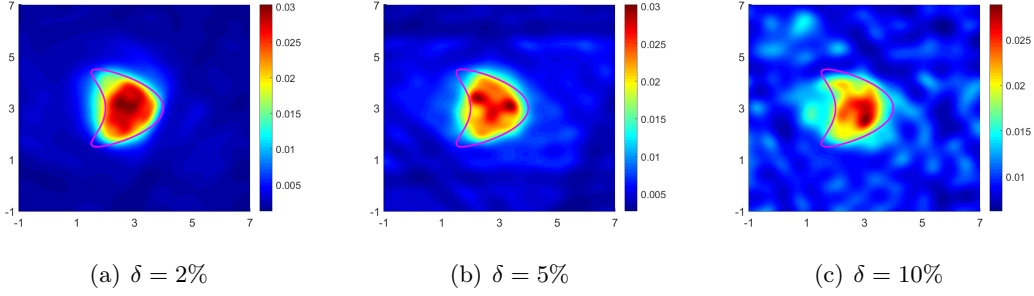


Figure 10: Reconstructions of a kite-shaped source from 8 observation directions with $S = 3(t + 1)$ at different noise levels δ .

6.3 Reconstruction of a moving point source

In this section we show an interesting example for reconstructing the trajectory of a moving point source. Suppose that the time-dependent source function $S(x, t)$ takes the form

$$S(x, t) = S_0(x - a(t)) := \frac{1}{\sqrt{2\pi\eta}} e^{-\frac{|x_1 - a_1(t)|^2 + |x_2 - a_2(t)|^2}{2\eta}}, \quad t \in (0, t_{\max}), \quad \eta = 0.01. \quad (6.47)$$

Since the function $S_0 : \mathbb{R}^2 \rightarrow \mathbb{R}$ exponentially decays as $|x| \rightarrow \infty$, it can be regarded as an approximation of the Dirac distribution $\delta(x)$. Hence, $S(x, t)$ can be used to model a moving point source with a compact support. At the time-point $t = t_0$, the function $S(x, t_0)$ is an approximation of the delta distribution $\delta(x - a(t_0))$ as long as $\eta > 0$ is sufficiently small. Here, we take $a(t) = (a_1(t), a_2(t)) = (t, t)$, which represents the path of the moving source. Below we describe our reconstruction procedures. Using different time windows $(T_j, T_j + T)$ and taking the transforms

$$f_j(x, k) := \int_{T_j}^{T_j+T} S(x, t) e^{-ikt} dt, \quad x \in D, \quad k \in (0, k_{\max}), \quad j = 0, 1, \dots, J,$$

we can get different wave-number-dependent source terms f_j , where $T = t_{\max}/J$ and $T_j = jT$. Denote by $\{w_j^\infty(\hat{x}_l, k) : l = 1, 2, \dots, M, k \in (0, k_{\max})\}$ the sparse far-field measurement data corresponding to f_j in the frequency domain. We want to determine the support of source functions $x \mapsto S(x, T_j)$ for $j = 1, 2, \dots, J$, which will approximate the trajectory function $t \mapsto a(t)$. For every time window $(T_j, T_j + T)$, we use the a test vector of the form (e.g., (6.46))

$$\phi_y^{(\hat{x})} := \left(\frac{i}{T\tau_1} (e^{-i\tau_1(T_j+T)} - e^{-i\tau_1 T_j}) e^{-i\tau_1 \hat{x} \cdot y}, \dots, \frac{i}{T\tau_N} (e^{-i\tau_N(T_j+T)} - e^{-i\tau_N T_j}) e^{-i\tau_N \hat{x} \cdot y} \right) \in \mathbb{C}^N.$$

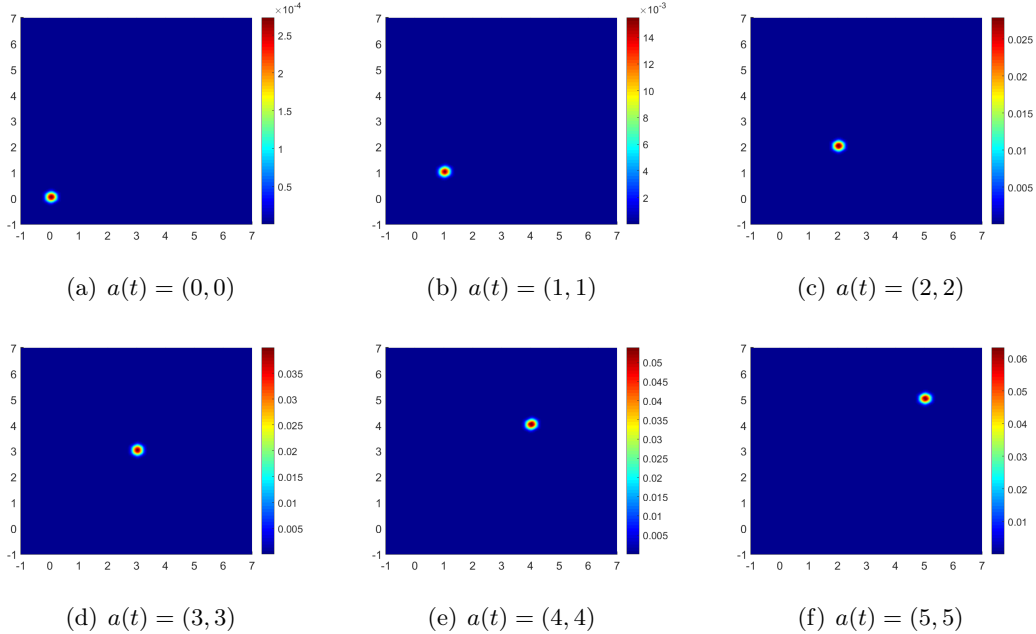


Figure 11: Reconstructions for a point source moving from $(0, 0)$ to $(5, 5)$ along a straight line.

In Fig.11, we reconstruct the trajectory of the moving point source from $t = 0$ to $t = 5$ by taking $T = 0.05$. It is clear that for at the time point T_j , the location $a(T_j)$ of the source function $S(x, T_j)$ can be roughly determined. The image in Fig.12 (a) is obtained by taking the sum of the indicator functions for each f_j . It is clearly shown that the trajectory of a point source moving from $(0, 0)$ to $(6, 6)$ along a straight line is nicely reconstructed. The resolutions for recovering the location of each source f_j are different, because the values of the indicator function at $t = 0$ are relatively small in comparison with those of indicators at other time points. Fig.12 (b) is retrieved from a normalized indicator function of the form

$$W(y) = \sum_{j=1}^J \frac{W_j(y)}{\max\{|W_j(y)| : y \in \Omega\}} \quad (6.48)$$

where W_j denotes the indicator function for imaging f_j and $\Omega = [-1, 7] \times [-1, 7]$ is our search region. In Fig.13 we change the Fourier time window to the form $(t, t+T)$ with different t and T . Consequently, the trajectory $\{a(s) : s \in (t, t+T)\}$ corresponding to this long time window can also be well reconstructed. These numerical tests are performed with 3 observation directions in Figs 11 and 12 and using 5 observation directions in Fig.13.

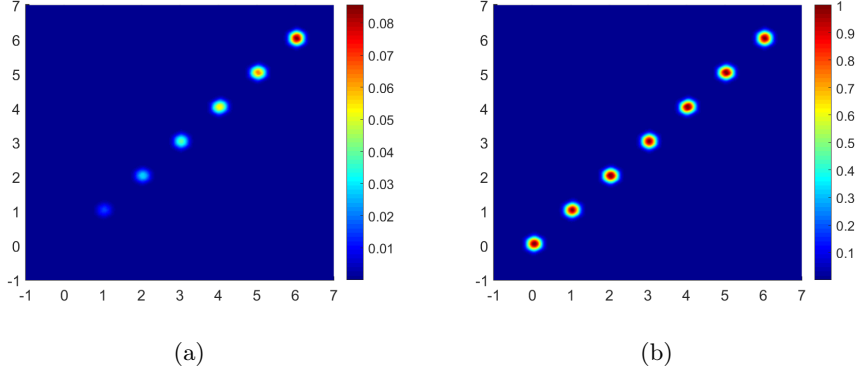


Figure 12: Reconstructions of a moving point source from $(0, 0)$ to $(6, 6)$ along a straight line. The time windows are taken as (T_j, T) with $T_j = 0, 1, \dots, J$ ($J = 6$) and $T = 0.05$. The right figure is based on the normalized indicator function (6.48).

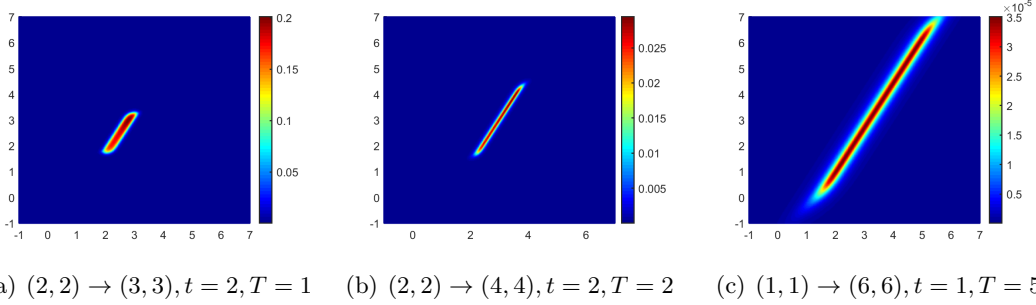


Figure 13: Reconstructions of a moving point source using different time windows $(t, t + T)$. The path $\{a(s) = (s, s) : s \in (t, t + T)\}$ has been illustrated.

6.4 Numerical implements with near-field measurements in \mathbb{R}^3

In this subsection, we present numerical reconstructions of the source support D from the multi-frequency near-field measurements $\{w(x_j, k) : x_j \in \partial B_R, k \in (k_{\min}, k_{\max}), j = 1, 2, \dots, M\}$ at sparse observation points. In view of Corollary 4.1, the smallest annular domain containing the source support and centered at x can be reconstructed with the indicator function $\widetilde{W}^{(x)}(y)$ in (4.37). The source support D can be imaged by plotting the truncated indicator

$$\widetilde{W}(y) := \left[\sum_{j=1}^M \sum_{n=1}^N \frac{|\tilde{\phi}_y^{(x_j)} \cdot \tilde{\psi}_n^{(x_j)}|^2}{|\tilde{\lambda}_n^{(x_j)}|} \right]^{-1}, \quad y \in \mathbb{R}^3. \quad (6.49)$$

In the following numerical examples, the frequency band is also taken as $(0, 16\pi/6)$ with $k_{\max} = 16\pi/6$, $N = 16$ and $\Delta k = \pi/6$.

Example 1 In this example, we use the indicator function $\widetilde{W}^{(x)}(y)$ of (4.37) to reconstruct the annular $\widetilde{K}_D^{(x)}$ for a cube. We take the temporal and spatial dependent source functions to be

$F(x, t) = (x_1^2 + x_2^2 + x_3^2 + 1)(t + 1)$ and the support of the source is assumed to be $D \times (t_{\min}, t_{\max})$. The cube D is defined by (see Fig.14 (a))

$$D = \{(x_1, x_2, x_3) : |x_1| < 0.5, |x_2| < 0.5, |x_3| < 0.5\}.$$

We take $t_{\min} = 0$, $t_{\max} = 0.1$ and set the measurement point at $(1.5, 0, 0)$. Then $\widetilde{W}^{(x)}(y)$ is plotted over the searching domain $[-1.5, 1.5]^3$ in Fig.14 (b) and (c). We present a slice of the reconstruction at $y_2 = 0$ in Fig.14 (b), from which we conclude that the cross of the plane $y_2 = 0$ with the smallest annular containing the square (in pink) and centered at $x = (1.5, 0, 0)$ is nicely reconstructed. Fig.14 (c) illustrates an iso-surface of the reconstruction at the iso-level 7×10^{-3} . The iso-surfaces perfectly enclose the cube-shaped support.

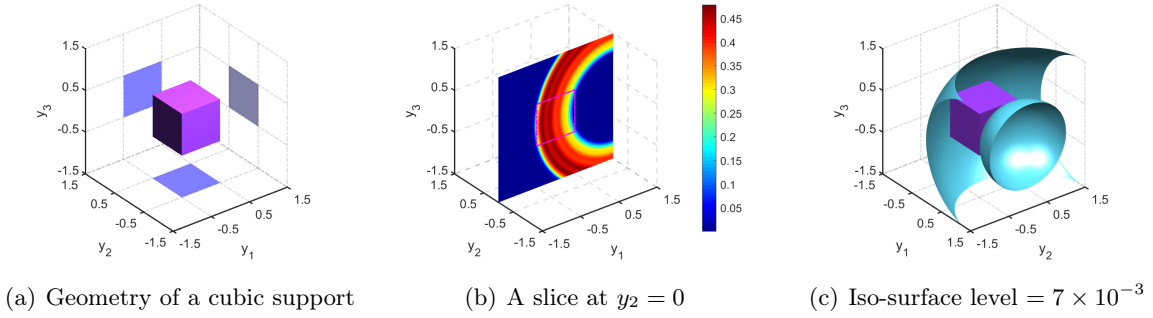


Figure 14: Reconstructions of a cube from the data measured at one observation point $(1.5, 0, 0)$. The Fourier transform window is $(t_{\min}, t_{\max}) = (0, 0.1)$.

Example 2 We continue **Example 1** with multiple observation points. A visualization of the indicator function $\widetilde{W}(y)$ in (6.49) is shown in Fig.15 with six observation points $\{(1.5, 0, 0), (-1.5, 0, 0), (0, 1.5, 0), (0, -1.5, 0), (0, 0, 1.5), (0, 0, -1.5)\}$. Fig.15 (a) presents an iso-surface of the reconstruction at the iso-level 2×10^{-2} and the projections of the images onto the oy_1y_2 , oy_1y_3 and oy_2y_3 planes. It is clearly shown that projections are all squares $[-0.5, 0.5]^2$, justifying the accuracy of our 3D reconstructions. Fig.15 (b) and (c) illustrate slices of the reconstructions at the planes $y_2, y_3 = 0$ and $y_1, y_2 = 0$ using the data at six observation points. These slices also confirm the accuracy of the 3D reconstructions.

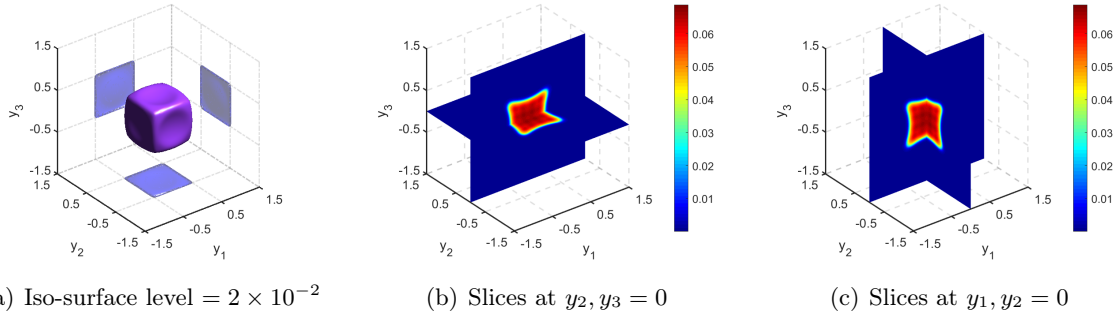


Figure 15: Reconstructions of a cube from six observation points. The Fourier transform window is $(0, 0.1)$.

In Figs 16 - 18, we show iso-surfaces and slices of the 3D reconstruction of the cubic source with a longer radiating period (t_{\min}, t_{\max}). Different Fourier transform windows from the data measured at six observation points are used. We choose the radiating period (resp. Fourier transform window) as $(0, 1)$ in Fig.16, as $(0, 3)$ in Fig.17 and as $(0, 5)$ in Fig.18. It can be observed that, even for a long duration $T = t_{\max} - t_{\min}$, satisfactory inversions for capturing the shape and location of the source can be achieved by taking different iso-surface levels. We also present some slices of the reconstructions, which all confirm effectiveness of our algorithm.

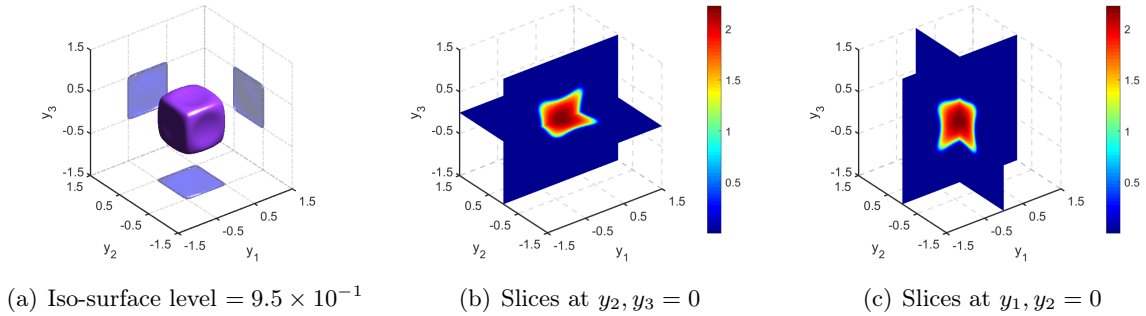


Figure 16: Reconstructions of a cube from six observation points. The Fourier transform window is $(0, 1)$.

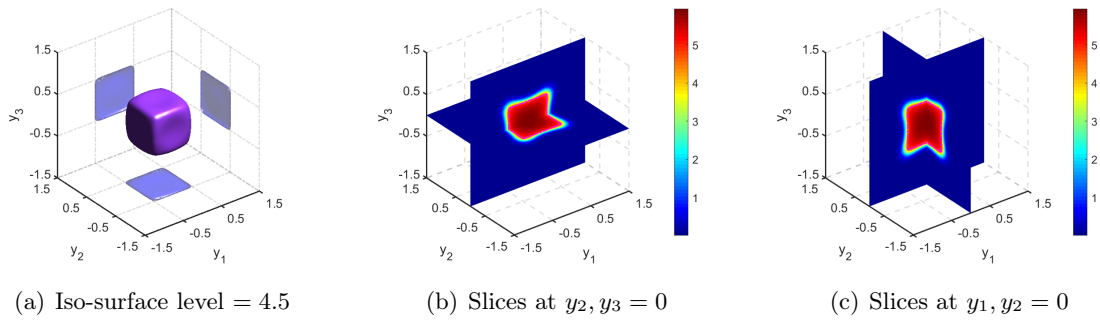


Figure 17: Reconstructions of a cube from six observation points. The Fourier transform window is $(0, 3)$.

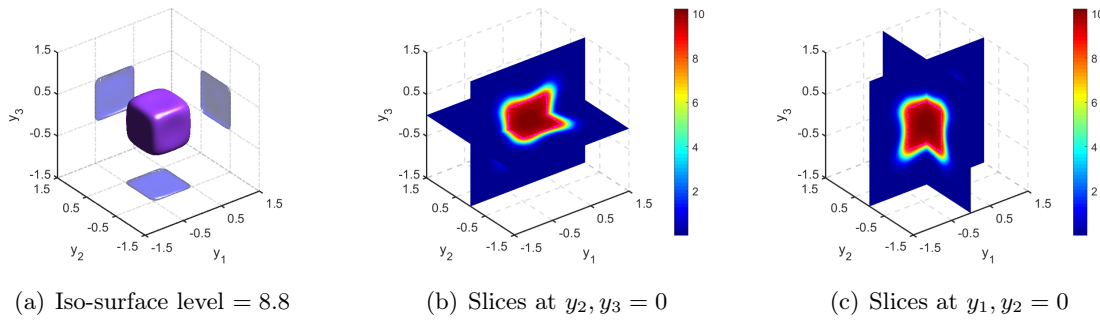


Figure 18: Reconstructions of a cube with six observation points. The Fourier transform window is $(0, 5)$.

Acknowledgements

G. Hu acknowledges the hospitality of the Institute for Applied and Numerical Mathematics, Karlsruhe Institute of Technology and the support of Alexander von Humboldt-Stiftung. Special thanks are given to R. Griesmaier for stimulating discussions. The work of G. Hu is partially supported by the National Natural Science Foundation of China (No. 12071236) and the Fundamental Research Funds for Central Universities in China (No. 63213025).

References

- [1] C. Alves, R. Kress, and P. Serranho, Iterative and range test methods for an inverse source problem for acoustic waves, *Inverse Problems*, 25 (2009): 055005.
- [2] A. Alzaalig, G. Hu, X. Liu and J. Sun, Fast acoustic source imaging using multi-frequency sparse data, *Inverse Problems*, 36 (2020): 025009.

- [3] G. Bao, P. Li, J. Lin and F. Triki, Inverse scattering problems with multi-frequencies, *Inverse Problems*, 31 (2015): 09300.
- [4] G. Bao, J. Lin, and F. Triki, A multi-frequency inverse source problem, *J. Differential Equations*, 249 (2010): 3443–3465.
- [5] G. Bao, S. Lu, W. Rundell and B. Xu, A recursive algorithm for multi-frequency acoustic inverse source problems, *SIAM J. Numer. Anal.*, 53 (2015): 1608-1628.
- [6] N. Bleistein and J. Cohen, Nonuniqueness in the inverse source problem in acoustics and electromagnetics, *J. Math. Phys.*, 18 (1977): 194–201.
- [7] E. Blasten, Nonradiating sources and transmission eigenfunctions vanish at corners and edges, *SIAM J. Math. Anal.*, 6 (2018): 6255–6270.
- [8] J. Cheng, V. Isakov and S. Lu, Increasing stability in the inverse source problem with many frequencies, *J. Differential Equations*, 260 (2016): 4786-4804.
- [9] A. J. Devaney and E. Wolf, Radiating and non-radiating classical current distributions and the fields they generate, *Phys. Rev. D*, 8 (1973): 1044-7.
- [10] A. Devaney, G. Sherman Nonuniqueness in inverse source and scattering problems *IEEE Trans. Antennas Propag.*, 30 (1982): 1034-1037.
- [11] M. Eller and N. Valdivia, Acoustic source identification using multiple frequency information, *Inverse Problems*, 25 (2009): 115005.
- [12] A. C. Fannjiang, T. Strohmer, and P. Yan, Compressed remote sensing of sparse objects, *SIAM J. Imaging Sci.*, 3 (2010): 595-618.
- [13] R. Griesmaire and C. Schmiedecke, A Factorization method for multifrequency inverse source problem with sparse far-field measurements, *SIAM J. Imaging Sciences*, 10 (2017): 2119-2139.
- [14] R. Griesmaier, Multi-frequency orthogonality sampling for inverse obstacle scattering problems, *Inverse Problems*, 27 (2011): 085005.
- [15] R. Griesmaier and M. Hanke, Multifrequency impedance imaging with multiple signal classification, *SIAM J. Imaging Sci.*, 8 (2015): 939-967.
- [16] R. Griesmaier, M. Hanke, and T. Raasch, Inverse source problems for the Helmholtz equation and the windowed Fourier transform, *SIAM J. Sci. Comput.*, 34 (2012): A1544-A1562.
- [17] R. Griesmaier, M. Hanke, and T. Raasch, Inverse source problems for the Helmholtz equation and the windowed Fourier transform II, *SIAM J. Sci. Comput.*, 35 (2013): A2188-A2206.

- [18] R. Griesmaier, M. Hanke and J. Sylvester, Far field splitting for the Helmholtz equation, *SIAM Journal on Numerical Analysis*, 52 (2014): 343-362.
- [19] R. Griesmaier and C. Schmiedecke, A multifrequency MUSIC algorithm for locating small inhomogeneities in inverse scattering, *Inverse Problems*, 33 (2017): 035015
- [20] G. Hu and J. Li, Uniqueness to inverse source problems in an inhomogeneous medium with a single far-field pattern, *SIAM J. Math. Anal.*, 52 (2020): 5213-5231.
- [21] G. Hu, Y. Kian, P. Li and Y. Zhao, Inverse moving source problems in electrodynamics. *Inverse Problems*, 35 (2019): 075001.
- [22] G. Hu and Y. Kian, Uniqueness and stability for the recovery of a time-dependent source in elastodynamics, *Inverse Problems and Imaging*, 14 (2020): 463-487.
- [23] G. Hu, Y. Kian and Y. Zhao, Uniqueness to some inverse source problems for the wave equation in unbounded domains, *Acta Mathematicae Applicatae Sinica, English Series*, 36 (2020): 134-150.
- [24] M. Ikehata, Reconstruction of a source domain from the Cauchy data, *Inverse Problems*, 15 (1999): 637-645.
- [25] X. Ji, X. Liu and B. Zhang, Inverse acoustic scattering with phaseless far field data: uniqueness, phase retrieval, and direct sampling methods, *SIAM J. Imaging Sci.*, 12 (2019): 1163-1189.
- [26] X. Ji, X. Liu and B. Zhang, Target reconstruction with a reference point scatterer using phaseless far field patterns, *SIAM J. Imaging Sci.*, 12 (2019): 372-391.
- [27] X. Ji, X. Liu and B. Zhang, Phaseless inverse source scattering problem: phase retrieval, uniqueness and direct sampling methods, *J. Comput. Phys. X*, 1 (2019): 100003.
- [28] A. Kirsch, Characterization of the shape of a scattering obstacle using the spectral data of the far field operator, *Inverse Problems*, 14 (1998): 1489-1512.
- [29] A. Kirsch and N. Grinberg, *The Factorization Method for Inverse Problems*, Oxford University Press, Oxford, UK, 2008.
- [30] S. Kusiak and J. Sylvester, The scattering support, *Comm. Pure Appl. Math.*, 56 (2003): 1525-1548.
- [31] P. Li and G. Yuan, Increasing stability for the inverse source scattering problem with multifrequencies, *Inverse Problems and Imaging*, 11 (2017): 745-759.

- [32] G. Ma and G. Hu, Factorization method with one plane wave: from model-driven and data-driven perspectives, *Inverse Problems*, 38 (2022): 015003.
- [33] A. Kirsch, The MUSIC algorithm and the factorization method in inverse scattering theory for inhomogeneous media, *Inverse Problems*, 18 (2002): 1025-1040.
- [34] R. Potthast, A study on orthogonality sampling, *Inverse Problems*, 26 (2010): 074015.
- [35] J. Sylvester, Notions of support for far fields, *Inverse Problems*, 22 (2006): 1273–1288.
- [36] J. Sylvester and J. Kelly, A scattering support for broadband sparse far field measurements, *Inverse Problems*, 21 (2005): 759-771.
- [37] D. Zhang and Y. Guo, Fourier method for solving the multi-frequency inverse source problem for the Helmholtz equation, *Inverse Problems*, 31 (2015): 035007.